



1 **Understanding mesoscale convective processes over the Congo Basin using the Model**  
2 **for Prediction Across Scales-Atmosphere (MPAS-A)**

3

4 **Siyu Zhao<sup>1</sup>, Rong Fu<sup>1,2</sup>, Kelly Núñez Ocasio<sup>3</sup>, Robert Nystrom<sup>4</sup>, Cenlin He<sup>5</sup>, and Jiaying**  
5 **Zhang<sup>6</sup>**

6 <sup>1</sup>Joint Institute for Regional Earth System Science & Engineering, University of California, Los  
7 Angeles, Los Angeles, CA, USA

8 <sup>2</sup>Department of Atmospheric and Oceanic Sciences, University of California, Los Angeles, Los  
9 Angeles, CA, USA

10 <sup>3</sup>Department of Atmospheric Sciences, Texas A&M University, College Station, TX, USA

11 <sup>4</sup>Department of Earth, Atmosphere, and Climate, Iowa State University, Ames, IA, USA

12 <sup>5</sup>Research Applications Laboratory, NSF National Center for Atmospheric Research (NCAR),  
13 Boulder, CO, USA.

14 <sup>6</sup>Agroecosystem Sustainability Center, Institute for Sustainability, Energy, and Environment,  
15 University of Illinois Urbana-Champaign, Urbana, IL, USA

16

17

18 Correspondence: Siyu Zhao (siyu\_zhao@atmos.ucla.edu)



19 **Abstract**

20           The Congo Basin in Central Africa is one of three convective centers in the tropics,  
21 characterized by a high proportion of precipitation produced by mesoscale convective systems  
22 (MCSs). However, process-level understanding of these systems and their relationship to  
23 environmental factors over the Congo Basin remains unclear, largely due to scarce in-situ  
24 observations. This study employs the Model for Prediction Across Scales–Atmosphere (MPAS-  
25 A), a global cloud-resolving model, to investigate MCSs in this region. Compared to satellite-  
26 observed brightness temperature ( $T_b$ ), MPAS-A realistically simulates key MCS features,  
27 allowing a detailed comparison between two mesoscale convective complex (MCC) cases: one  
28 over the southern mountainous region (MCC-south) and the other over the northern lowland forests  
29 (MCC-north). MCC-south is larger, longer-lived, and moves a longer distance than MCC-north.  
30 Our analysis shows that MCC-south is supported by higher thermodynamic energy and more  
31 favorable vertical wind shear ahead of the system. The shear extends up to 400 km, explains up to  
32 65% of the  $T_b$  variance, and is well balanced by a moderately strong cold pool. In contrast, MCC-  
33 north features weaker, localized shear near the center and a stronger cold pool. The African  
34 Easterly Jet helps maintain the shear in both cases, but an overly strong jet may suppress low-level  
35 westerlies and weaken convection. These results show how latitude and topography modulate  
36 environmental influences on Congo Basin MCS developments. The findings underscore the value  
37 of global cloud-resolving models in data-sparse regions for understanding convective systems and  
38 their impacts on weather extremes and societal risks.



## 39 1 Introduction

40 The tropical rainforest rainfall is critical in regulating global weather and climate patterns,  
41 sustaining more than 50% of the global biospecies, and providing resources for local communities  
42 and the broader global ecosystem. Rainfall in tropical rainforests is primarily driven by convective  
43 processes, with mesoscale convection systems (MCSs) playing a major role (e.g., Trismidianto et  
44 al., 2017; Rehbein et al., 2019; Andrews et al., 2024). MCSs are large, organized clusters of  
45 thunderstorms that produce significant rainfall and severe weather, persisting for several hours  
46 when they develop and mature through the aggregation of cumulonimbus clouds (Houze 2004,  
47 2018).

48 Recent studies have advanced the understanding of MCSs, including their classification,  
49 dynamics, and links to large-scale circulations and atmospheric chemistry (e.g., Zuluaga & Houze,  
50 2013; Peters & Schumacher, 2016; Clavner et al., 2018; Houze, 2018; Schumacher & Rasmussen,  
51 2020; Chakraborty et al., 2023), but challenges remain in understanding the physical mechanisms  
52 that control MCSs characteristics, such as their lifetimes, geographic variation and evolution  
53 across land surfaces influenced by varying atmospheric dynamics (Houze, 2018). In the  
54 midlatitudes, MCS research has focused on their strong seasonality, role in severe weather, and  
55 interactions with low-level jets, frontal systems, and extratropical cyclones (e.g., Kunkel et al.,  
56 2012; Smith et al., 2012; Rasmussen et al., 2016; Feng et al., 2019). In the tropics, MCSs are  
57 commonly observed in regions such as the Indo-Pacific warm pool, the Amazon, and tropical  
58 Africa, with numerous studies examining their interactions with the Madden-Julian Oscillation  
59 (MJO), monsoons, and tropical cyclones (e.g., Laing & Fritsch, 1997; Lee et al., 2008; Barnes &  
60 Houze, 2013; Sullivan et al., 2019; Chen et al., 2022).

61 In tropical Africa, MCSs are linked to African easterly waves and can contribute to tropical  
62 cyclone genesis through favorable West African Monsoon conditions and proper phasing between  
63 convective heating and the wave's vorticity center (e.g., Sultan et al., 2003; Hopsch et al., 2010;  
64 Núñez Ocasio et al., 2020a, 2020b, 2021; Mayta et al., 2025). The Congo Basin, located in Central  
65 Africa, occupies only 10% of Africa's landmass, but supplies 30% of the continent's water  
66 resources by housing the world's second-largest river by discharge volume (Brummet et al., 2009;  
67 N'kaya et al., 2022). It houses one of the three core regions of convection in the tropics and the  
68 world's second-largest rainforest (Washington et al., 2013). The Congo Basin experiences some  
69 of the world's most intense thunderstorms, often associated with MCSs, which contribute to over  
70 80% of the region's total rainfall—significantly higher than in other tropical regions (e.g., Mohr  
71 et al., 1999; Nicholson, 2022; Andrews et al., 2024). In recent years, extreme rainfall-driven runoff  
72 anomalies have intensified river flood hazards across the Congo Basin, causing major economic  
73 losses and around 2,000 deaths annually from river-related incidents (CICOS, 2012; Tshimanga et  
74 al., 2016; Schumann et al., 2022). Thus, studying MCSs and rainfall in this region is crucial for  
75 agriculture, river navigation, economic stability, and overall human well-being in central sub-  
76 Saharan Africa (Tshimanga et al., 2022).

77 Previous studies have widely evaluated the observed characteristics, including temporal  
78 frequency, spatial variability, moving tracks, and overall statistics, of equatorial African or Congo  
79 Basin MCSs, as well as their connections to rainfall, lightning, and environmental factors (e.g.,  
80 Laing & Fritsch, 1993; Nguyen & Duvel, 2008; Jackson et al., 2009; Laing et al., 2011; Hartman,  
81 2020; Mba et al., 2022; Nicholson, 2022; Kigotsi et al., 2022; Solimine et al., 2022; Andrews et  
82 al., 2024). The seasonality of Congo Basin MCS occurrence indicates that MCS activity and  
83 associated rainfall migrate periodically across the equator, occurring southward in boreal winter



84 and northward in boreal summer (Jackson et al., 2009; Andrews et al., 2024). Although the  
85 migration is often linked to the Intertropical Convergence Zone, recent studies suggest that rainfall  
86 and MCS activity over the Congo Basin involve more complex processes, as heavy rainfall may  
87 occur without the typical low-level convergence (Yang et al., 2015; Nicholson, 2018). MCSs in  
88 the Congo Basin typically exhibit westward propagation, with a substantial number originating  
89 along the lee side of the high terrain of the Great Rift Valley (Jackson et al., 2009; Laing et al.,  
90 2011; Hartman, 2020). This westward propagation is influenced by moderate low-level shear  
91 associated with the African Easterly Jet (AEJ), as well as the modulation of convectively coupled  
92 Kelvin waves and the MJO (Nguyen & Duvel, 2008; Jackson et al., 2009; Laing et al., 2011).

93 However, due to sparse in-situ observations (Nicholson et al., 2018; Tshimanga et al., 2022)  
94 and the low-resolution of reanalysis data ( $0.25^\circ$  over Central Africa), the relationship between  
95 Congo Basin MCSs and environmental factors (e.g., vertical shear) has largely been explored from  
96 a climate perspective, with limited quantitative analyses based on MCS moving tracks.  
97 *Quantitative, process-level understanding of Congo Basin MCSs and their relationships with*  
98 *environmental factors—particularly those based on MCS tracks from a weather perspective—*  
99 *remains limited.* Such weather timescale studies necessitate model simulations capable of  
100 resolving mesoscale circulations (Laing et al., 2011).

101 Although Congo Basin rainfall has been simulated by regional and global models (e.g.,  
102 Washington et al., 2013; Aloysius et al., 2016; Creese & Washington, 2016, 2018; Creese et al.,  
103 2019; Fotso-Kamga et al., 2020), few studies have utilized models, especially high-resolution  
104 cloud-resolving models, to simulate individual Congo Basin MCSs. Such models are essential for  
105 accurately representing mesoscale convective processes. One of the studies focusing on Congo  
106 Basin MCSs using a high-resolution cloud-resolving model was conducted by Raghavendra et al.  
107 (2022), who utilized the Weather Research and Forecasting (WRF) at 4 km with convection-  
108 permitting setup and perturbed topography with varying heights for November 2014. Their study  
109 showed that brightness temperature ( $T_b$ ) is well simulated in the control run, indicating the  
110 capability of WRF at a high resolution in simulating a key feature of MCSs over the Congo Basin.  
111 The important relationships between tropical MCSs/rainfall and topography have been  
112 documented in their study and others (e.g., Hamilton et al., 2017, 2020). However, Congo Basin  
113 MCSs were not explicitly identified, tracked, or classified using a tracking algorithm, and the  
114 quantitative influences of key environmental factors on their developments along the track were  
115 not examined in previous studies.

116 In the past decade, global cloud-resolving models have been developed, such as the Model  
117 for Prediction Across Scales–Atmosphere (MPAS-A) (Skamarock et al. 2012). MPAS-A  
118 incorporates physics schemes from WRF but offer the option of using a variable-resolution global  
119 Voronoi mesh, which can avoid nesting techniques or usual pole-related grid transformations and  
120 improves computational performance over traditional regional cloud-resolving models. Recently,  
121 both global and regional configurations of MPAS-A have been applied to the African and Atlantic  
122 regions during the tropical cyclogenesis of Hurricane Helene (2006) (Núñez Ocasio & Rios-  
123 Berrios, 2023; Núñez Ocasio & Dougherty, 2024; Núñez Ocasio et al., 2024). For example,  
124 MPAS-A has been used to examine the role of moisture in the AEJ and monsoon dynamics, rainfall  
125 shifts, easterly wave–MCS interactions related to tropical cyclogenesis, and the impacts of a  
126 warmer, moister climate on these multiscale tropical systems (Núñez Ocasio & Dougherty, 2024).

127 Therefore, we take the advantage of the cloud-resolving capability and global Voronoi mesh  
128 offered by MPAS-A to gain the process-level understanding of Congo Basin MCSs and their



129 connections to environmental factors. From November 2023 to January 2024, the Democratic  
130 Republic of the Congo and Congo-Brazzaville experienced their worst flooding in 60 years  
131 (Davies, 2024; Joachim et al., 2024). We apply satellite observations and MPAS-A to analyze  
132 MCSs from November 21 to 25, 2023. We then apply the Tracking Algorithm for Mesoscale  
133 Convective Systems (TAMS; Núñez Ocasio et al., 2020b; Núñez Ocasio & Moon, 2024) to  
134 objectively identify, track, and classify MCSs over the Congo Basin. TAMS offers capabilities  
135 comparable to other tracking methods but stands out due to its unique tracking approach, MCS  
136 classification scheme, and consideration of background flow. Once MCS tracks are obtained, we  
137 focus on long-lasting (over 15 hours) MCS events and use MPAS-A to quantify the role of key  
138 environmental factors in MCS developments. The remainder of the paper is organized as follows.  
139 Data and methodology are described in Section 2. Section 3.1 discusses Congo Basin rainfall and  
140 MCS statistics. Section 3.2 evaluates model's ability to simulate mesoscale convective processes.  
141 The role of vertical wind shear and the AEJ is discussed in Section 3.3. A summary and additional  
142 discussion are provided in Section 4.

## 143 **2 Data and methodology**

### 144 **2.1 Data**

145 We use hourly data to examine Congo Basin MCSs for the period of November 21–25,  
146 2023. The National Centers for Environmental Prediction (NCEP)/Climate Prediction Center  
147 (CPC) L3 Half Hourly 4km Global Merged infrared (IR) Tb data (Janowiak et al., 2017) is used  
148 to detect MCSs. This Tb data has been widely used in tracking MCSs, especially over tropical  
149 regions (e.g., Feng et al., 2021, 2023a, 2025; Chen et al., 2023; Prein et al., 2024; Muetzelfeldt et  
150 al., 2025). Due to the sparsity of gauge networks over the Congo Basin in recent decades  
151 (Nicholson et al., 2018), we will mainly use satellite precipitation data. Since MCS detection  
152 requires high-resolution, sub-daily data, we analyze precipitation associated with identified MCSs  
153 using half-hourly precipitation data from the CPC Morphing Technique (CMORPH) Climate Data  
154 Record (CDR) with an 8 km horizontal resolution (Xie et al., 2019) and the Global Precipitation  
155 Measurement (GPM) Integrated Multi-satellite Retrievals (IMERG) Final Precipitation with a 0.1°  
156 horizontal resolution (Huffman et al., 2023).

157 In addition to hourly data, daily precipitation data are used to analyze daily and monthly  
158 precipitation over the Congo Basin. These datasets include CMORPH CDR (0.25° horizontal  
159 resolution, 1998–2024) (Xie et al., 2019), GPM IMERG Final Precipitation (0.1° horizontal  
160 resolution, 2001–2024) (Huffman et al., 2023), and the CPC Global Unified Gauge-Based  
161 Analysis of Daily Precipitation (0.5° horizontal resolution, 1979–2024) (Chen et al., 2008).  
162 Additionally, daily runoff data are obtained from the Global Land Data Assimilation System  
163 (GLDAS) Catchment Land Surface Model L4 (0.25° horizontal resolution, 2004–2024) (Li et al.,  
164 2020).

### 165 **2.2 Model configuration and simulations**

166 MPAS-A is a global cloud-resolving model representing a new category of atmospheric  
167 models and is a participant in DYAMOND, the first intercomparison project of such models  
168 (Stevens et al., 2019). It solves non-hydrostatic equations using kilometer-scale global meshes and  
169 simulates deep convection explicitly (Skamarock et al., 2012; Satoh et al., 2019). In this study, we  
170 use MPAS-A version 8 modified to output variables at 27 isobaric levels (Núñez Ocasio et al.,



171 2024). We use a variable-resolution, 60–3 km global mesh, and the Congo Basin is roughly within  
172 the 3 km domain (Fig. 1a). The model uses 55 vertical levels up to ~30 km height.

173 The model physics follows the standard mesoscale-reference suite incorporating the new  
174 scale-aware Tiedtke convection scheme, which is newly added to MPAS-A version 8 and suitable  
175 for a convection-permitting mesh with grid spacing below 10 km (Wang, 2022). The scale-aware  
176 Tiedtke scheme effectively reduces deep convection by decreasing the convective portion of total  
177 surface precipitation, and also ensures smooth handling of convection across mesh transition zones  
178 when applied to a variable mesh in MPAS-A (Wang, 2022). The other schemes of the physics suite  
179 include the WSM6 microphysics scheme (Hong & Lim, 2006), the Noah land surface scheme (Niu  
180 et al., 2011), the YSU boundary layer scheme (Hong et al., 2006), the Monin-Obukhov surface  
181 layer scheme (Jiménez et al., 2012), the RRTMG shortwave and longwave radiation scheme  
182 (Iacono et al., 2008), and the Xu-Randall subgrid cloud fraction scheme (Xu & Randall, 1996).

183 We use the European Centre for Medium-Range Weather Forecasts (ECMWF) fifth-  
184 generation reanalysis (ERA5; Hersbach et al., 2020), including a complete set of atmospheric  
185 pressure level and surface variables, to initialize model simulations. The experiments begin at 1200  
186 UTC on November 21, 2023, running for four days, with the first six hours discarded for spin-up.  
187 The model produces hourly outputs at 27 isobaric levels. In addition to the primary simulation  
188 discussed above, we have conducted additional simulations to ensure that our conclusions were  
189 not influenced by model stochasticity. In the sensitivity tests, random perturbations were added to  
190 the 1000-hPa potential temperature field following a Gaussian distribution with a standard  
191 deviation of 0.6 K, as in Núñez Ocasio et al. (2024). Since the results of the sensitivity tests closely  
192 resemble those of the unperturbed simulation, we present only the model simulation without  
193 random perturbations in this study.

### 194 2.3 MCS tracking

195 The Congo Basin MCS tracking is conducted objectively using the latest version of TAMS,  
196 an open-source, Python-based package for tracking and classifying MCSs (Núñez Ocasio & Moon,  
197 2024). Following the MCS tracking algorithm described in Núñez Ocasio et al. (2020b) and Núñez  
198 Ocasio & Moon (2024), hourly Tb contours are used to identify cloud elements (CEs), selecting  
199 235 K regions that contain embedded 219 K areas of at least 4,000 km<sup>2</sup>. In MPAS-A, Tb is derived  
200 from the model’s outgoing longwave radiation output following the method of Yang & Slingo  
201 (2001). MCS tracks are determined by linking CEs from the current time step to those from the  
202 previous step based on maximum CE polygon overlap. Once an MCS is identified and tracked, its  
203 complete trajectory is analyzed, allowing its entire lifespan to be assigned to a single classification.  
204 Table 1 shows the MCS classification criteria (e.g., Maddox, 1980; Evans & Shemo, 1996;  
205 Tsakrakilides & Evans, 2003; Núñez Ocasio et al., 2020b) used in TAMS, which includes four  
206 categories: mesoscale convective complex (MCC), convective cloud cluster (CCC), disorganized  
207 long-lived (DLL), and disorganized short-lived (DSL). TAMS outputs include the latitude and  
208 longitude centroids of 219 K and 235 K regions for each MCS at every time step, along with  
209 additional statistics such as area, duration, and mean precipitation for each identified MCS.

**Table 1.** Criteria to categorize MCS

Category	Size and temperature	Duration	Shape
----------	----------------------	----------	-------

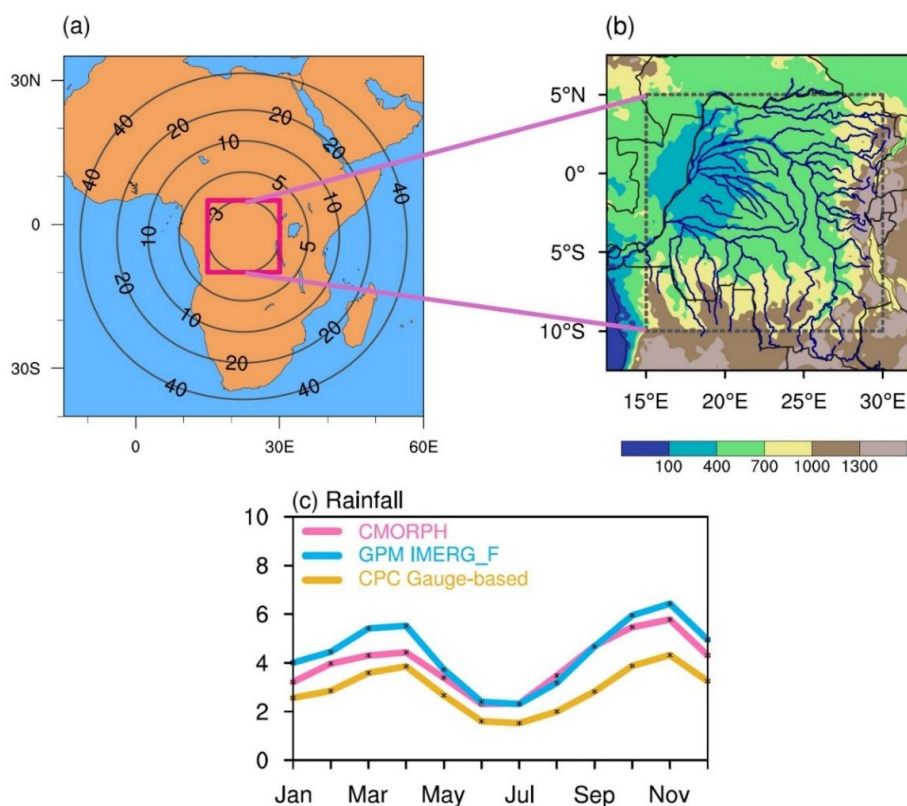


MCC	<219K region has area $\geq 25\,000\text{ km}^2$ <235K region has area $\geq 50\,000\text{ km}^2$	size definitions are met for $\geq 6\text{ h}$	$\varepsilon = \sqrt{1 - (b^2/a^2)} \leq 0.7$
CCC	<219K region has area $\geq 25\,000\text{ km}^2$	size definitions are met for $\geq 6\text{ h}$	n/a
DLL	<219K	sustains for $\geq 6\text{ h}$	n/a
DSL	<219K	sustains for $\leq 3\text{ h}$	n/a

210

211 **3 Results**

212 **3.1 Congo Basin rainfall and MCS statistics**



213

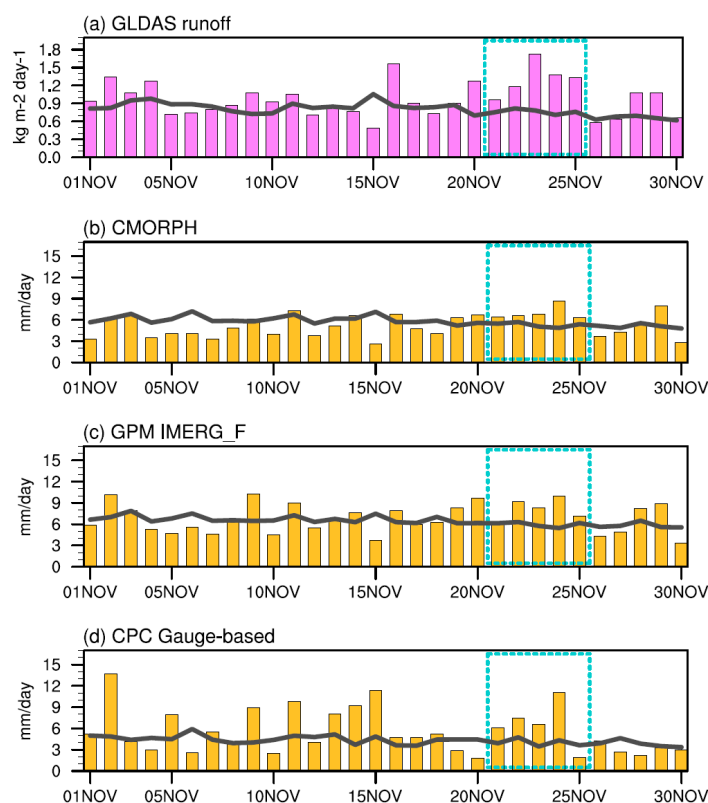
214 **Figure 1.** (a) Illustration of the 60–3 km global variable resolution mesh. Contours represent  
 215 resolution from 3 km to 40 km. The pink box represents the Congo Basin (10°S–5°N, 15°E–30°E),  
 216 which roughly has the resolution of 3 km. (b) The elevation (m) of the Congo Basin (within the  
 217 dashed box). Blue lines indicate rivers. (c) Climatology of the monthly mean basin-averaged  
 218 precipitation (mm/day) for three observed datasets. The climatological period for each dataset  
 219 corresponds to its available data range, as detailed in Section 2.1.

220



221 The Congo Basin spans a vast area across Central Africa, with elevation varying  
222 significantly. It primarily consists of lowlands in the west, central, and northern regions,  
223 surrounded by higher elevations in the south and east (Fig. 1b). It is home to a complex river  
224 system, dominated by the Congo River, the second largest in the world by discharge. The seasonal  
225 cycle of Congo Basin domain-averaged precipitation exhibits a biannual pattern, with the first peak  
226 occurring in March–April and the second in October–November (Fig. 1c). The satellite data  
227 generally show a higher daily precipitation rate compared to gauge-based data, a discrepancy that  
228 has been widely studied in comparisons with gauging station networks (e.g., Hughes, 2006). This  
229 biannual cycle is recognized as a key characteristic of Congo Basin rainfall (e.g., Washington et  
230 al., 2013; Pokam et al., 2014; Dyer et al., 2017), though it may be more pronounced south of the  
231 equator (Nicholson, 2022).

232 Between November 2023 and January 2024, the Democratic Republic of the Congo and  
233 Congo-Brazzaville experienced their worst flooding in 60 years (Davies, 2024; Joachim et al.,  
234 2024). Figure 2a shows the climatological daily mean runoff (line) and daily runoff in November  
235 2023 (bars), highlighting extreme runoff anomalies (up to 50% above the climatological mean)  
236 during November 21–25. All three rainfall datasets also exhibit consecutive days of positive  
237 precipitation anomalies, especially in GPM IMERG and CPC gauge-based data (Fig. 2b–d). Since  
238 MCSs account for approximately 80% of the total rainfall in the Congo Basin (e.g., Mohr et al.,  
239 1999; Nicholson, 2022; Andrews et al., 2024), this study focuses on the period mentioned above  
240 to improve the process-level understanding of MCSs in this region.



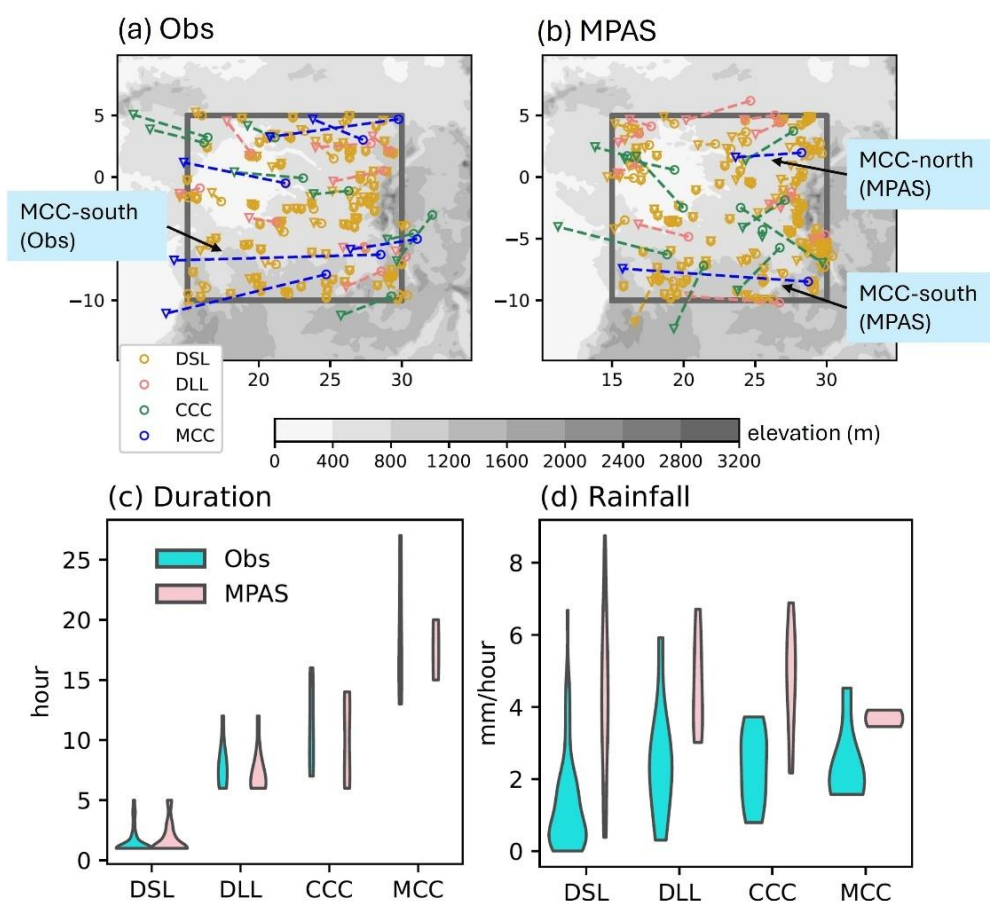
241



242 **Figure 2. (a)** Daily mean basin-averaged runoff (bars; kg/m<sup>2</sup>/day) from GLDAS from November  
 243 01, 2023, to November 30, 2023, overlaid by climatological runoff (gray line) during November.  
 244 The period analyzed in this study is within the turquoise box. **(b–d)** Same as **(a)**, but for  
 245 precipitation (mm/day) from three observational datasets. The climatological period for each  
 246 dataset corresponds to its available data range, as detailed in Section 2.1.

247

248 Following the method in Section 2, we apply TAMS to objectively identify, track, and  
 249 classify MCSs. Figure 3a displays all identified MCSs that passed through the Congo Basin during  
 250 the study period in observations. For simplicity, only the initial and final locations are shown.  
 251 Consistent with previous studies (Jackson et al., 2009; Laing et al., 2011; Hartman, 2020), most  
 252 MCSs propagate westward, with a substantial number originating in the lee side of the high terrain  
 253 of the Great Rift Valley. Following the strictest criteria in Table 1, MCCs generally initiate in the  
 254 eastern portion of the basin and propagate the longest distance; one MCC case even moves from  
 255 the eastern boundary to the western boundary. CCCs have the second-longest moving distances,  
 256 slightly longer than DLLs. By definition, DSLs are localized, with the shortest moving distances,  
 257 and they can occur over most areas of the basin.



258



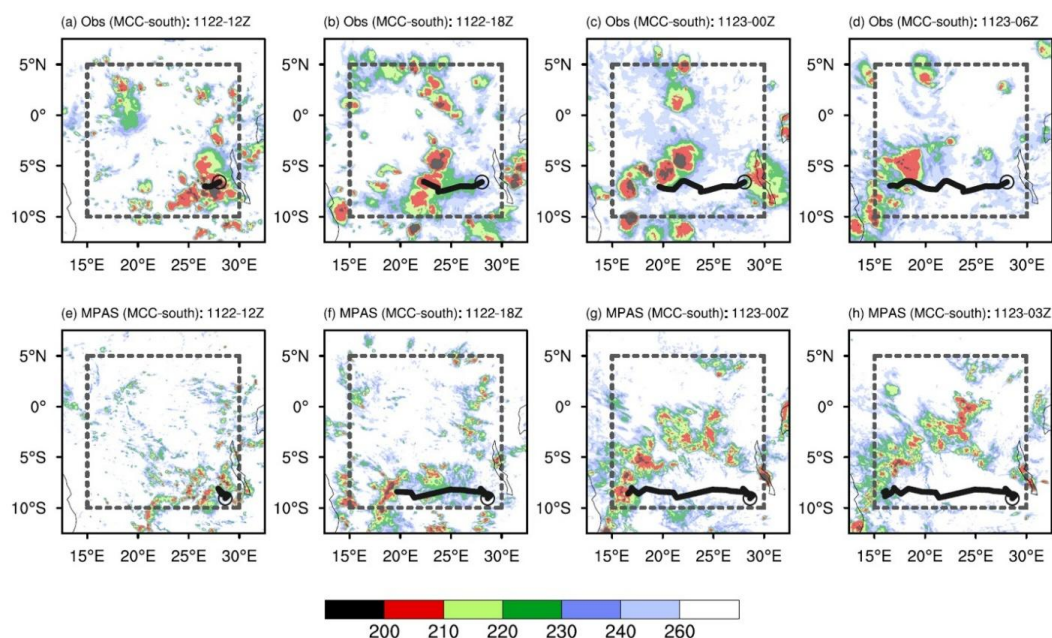
259 **Figure 3.** Initial (circles) and final (triangles) locations of each detected MCS during November  
260 21–25, 2023, based on (a) observations and (b) MPAS-A simulations. The four categories of MCS  
261 are represented by different colors. Dashed lines indicate the connection between initial and final  
262 locations but do not represent the actual MCS tracks. Shading represents elevation (m). The MCC  
263 cases analyzed in this study are marked. Violin plots of (c) duration (hours) and (d) mean  
264 precipitation (from CMORPH; mm/hour) within the 219 K contours for each MCS category in  
265 observations and MPAS-A simulations. The width of the violin plot indicates probability  
266 distribution.

267

### 268 3.2 Model's ability to simulate MCSs

269 In this section, we evaluate how well MPAS-A simulates MCSs by conducting simulations  
270 for November 21–25, 2023, as described in Section 2. We do not expect the model to capture every  
271 individual MCS track in MPAS-A, instead our goal is to assess whether long-duration or long-  
272 track MCS events and the overall MCS statistics are realistically represented. The model  
273 successfully simulates the general westward propagation of MCSs, but the number of MCC cases  
274 is lower than in observations (Fig. 3b). Notably, the long-track MCC case over the southern basin  
275 (referred to as MCC-south) is well captured in terms of spatial location. Figure 3c–d compares  
276 MCS characteristics between observations and model simulations. The MCS duration is well  
277 simulated, particularly for DSL, DLL, and CCC (Fig. 3c). MCCs typically last over 15 hours, with  
278 one observed case lasting 27 hours. The two simulated MCCs last 15 and 20 hours, respectively,  
279 consistent with observations. Compared to observations, the model overestimates rainfall for all  
280 four categories (Fig. 3d), likely due to stronger simulated convection and increased moisture  
281 convergence, consistent with previous studies (e.g., Raghavendra et al., 2022; Feng et al., 2023b,  
282 2025).

283 We compare the spatial distribution of the observed MCC-south case with that from  
284 MPAS-A simulations. The observed  $T_b$  shows that MCC-south originates from the Great Rift  
285 Valley (Fig. 4a), propagates westward during the late afternoon and evening (local time UTC  
286 +01:00 or +02:00, Fig. 4b–c), and weakens in the following morning (Fig. 4d). The mean area of  
287 the observed MCC-south (averaged across all time steps) is  $6.7 \times 10^5 \text{ km}^2$ , covering nearly 30% of  
288 the Congo Basin, and the mean area enclosed by the 219 K contours is  $3.2 \times 10^5 \text{ km}^2$ , approximately  
289 half of the total MCC area. The simulated MCC-south originates from the Great Rift Valley,  
290 though slightly farther south, and propagates westward across the Congo Basin (Fig. 4e–h). While  
291 the simulated  $T_b$  is more scattered and the mean MCC area is 12% smaller than observed, the  
292 model still successfully captures the timing and general location of MCC-south.

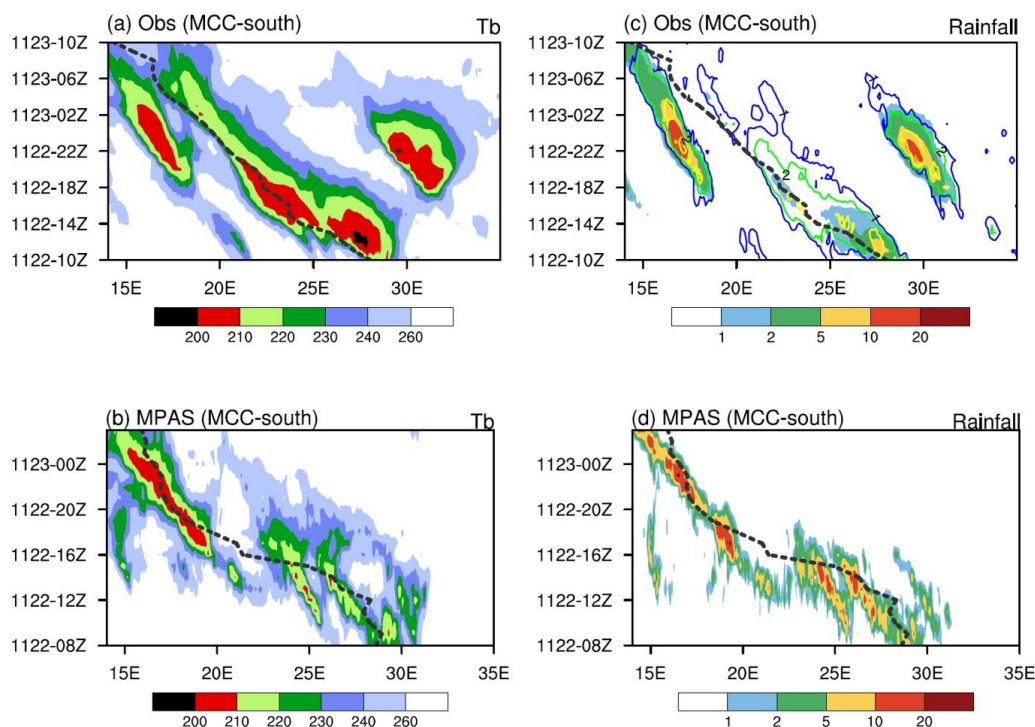


293

294 **Figure 4.** (a–d) MCC-south tracking of Tb (K) every 6 hours from NCEP/CPC data in  
 295 observations. The black line represents the MCC track, and the open circle denotes its initiation  
 296 location. (e–h) Same as (a–d), but for MPAS-A simulations.

297

298 To better understand the evolution of Tb and associated rainfall, we present the Hovmöller  
 299 diagram along the MCC track. Figure 5a illustrates the observed Tb evolution for MCC-south,  
 300 which originates near 29°E, featuring three centers (Tb < 210 K) along its path, excluding the one  
 301 east of 30°E, as it does not belong to MCC-south. The simulated Tb evolution shares a similar  
 302 pattern with observations, but during the initial stage, Tb magnitudes are smaller, and the Tb  
 303 pattern appears more scattered (Fig. 5b). The simulated MCC strengthens (Tb decreases)  
 304 significantly during the mid-stage of MCC-south (around 16Z), warranting further analyses to  
 305 investigate the underlying mechanisms. While rainfall from the two observations generally aligns  
 306 with Tb from NCEP/CPC data, CMORPH shows lower rainfall in the early–mid stages and higher  
 307 rainfall in the later stage (Fig. 5c). Consistent with Fig. 3d, the simulated rainfall magnitudes  
 308 exceed those in observations (Fig. 5d). The high rainfall magnitudes in cloud-resolving models  
 309 have also been observed in previous studies (e.g., Raghavendra et al., 2022; Feng et al., 2023b,  
 310 2025). Despite these differences, the results above suggest that MPAS-A shows promise in  
 311 simulating long-lived, long-track MCC over the Congo Basin.

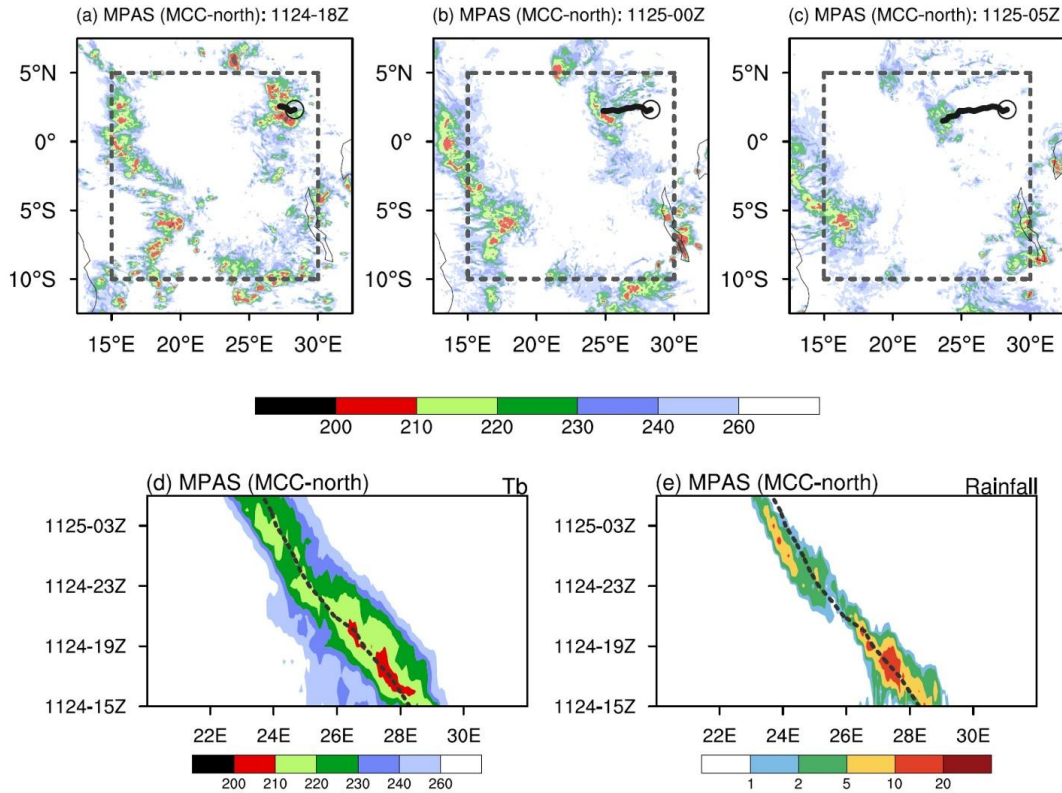


312

313 **Figure 5.** Hovmöller diagram for (a) 6°S–7.5°S averaged Tb (K) from NCEP/CPC data and (b)  
 314 8°S–9°S averaged Tb from MPAS-A simulations, along the track of MCC-south. The black dashed  
 315 line represents the MCC track. (c–d) Same as (a–b), but for precipitation (mm/hour). In (c), both  
 316 CMORPH CDR (shading) and GPM IMERG (contours; contour values: 1, 2, and 5 mm/hour)  
 317 precipitation are shown.

318

319 Next, we utilize the model to further understand mesoscale convective processes by  
 320 comparing two representative MCC cases, MCC-south and another MCC case over the northern  
 321 basin, referred to as MCC-north (Fig. 3b). MCC-north originates during the evening over the  
 322 northeastern boundary of the Congo Basin, where the elevation ranges from approximately 700 to  
 323 1000 m (Fig. 6a). The system then propagates westward through midnight (Fig. 6b) and weakens  
 324 over lowlands, where elevations drop to 400–700 m or lower, by early morning (Fig. 6c). The  
 325 mean area of the simulated MCC-north is about 22% of that of MCC-south, with a shorter lifecycle  
 326 of 15 hours compared to 20 hours for MCC-south. Additionally, its moving distance is  
 327 approximately 35% of that of MCC-south. Overall, MCC-north is smaller in size, shorter in  
 328 duration, and less extensive in movement compared to MCC-south. Figure 6d–e presents the  
 329 Hovmöller diagrams of Tb and rainfall along the MCC-north track. MCC-north intensifies rapidly  
 330 after its initiation, characterized by low Tb centers and rainfall exceeding 10 mm/hour during its  
 331 early stage (before 19Z). Contrary to MCC-south (Fig. 5b), the simulated MCC-north weakens  
 332 (Tb increases) significantly from the mid-stage (around 21Z). We investigate the mechanisms  
 333 responsible for such difference in Section 3.3.



334

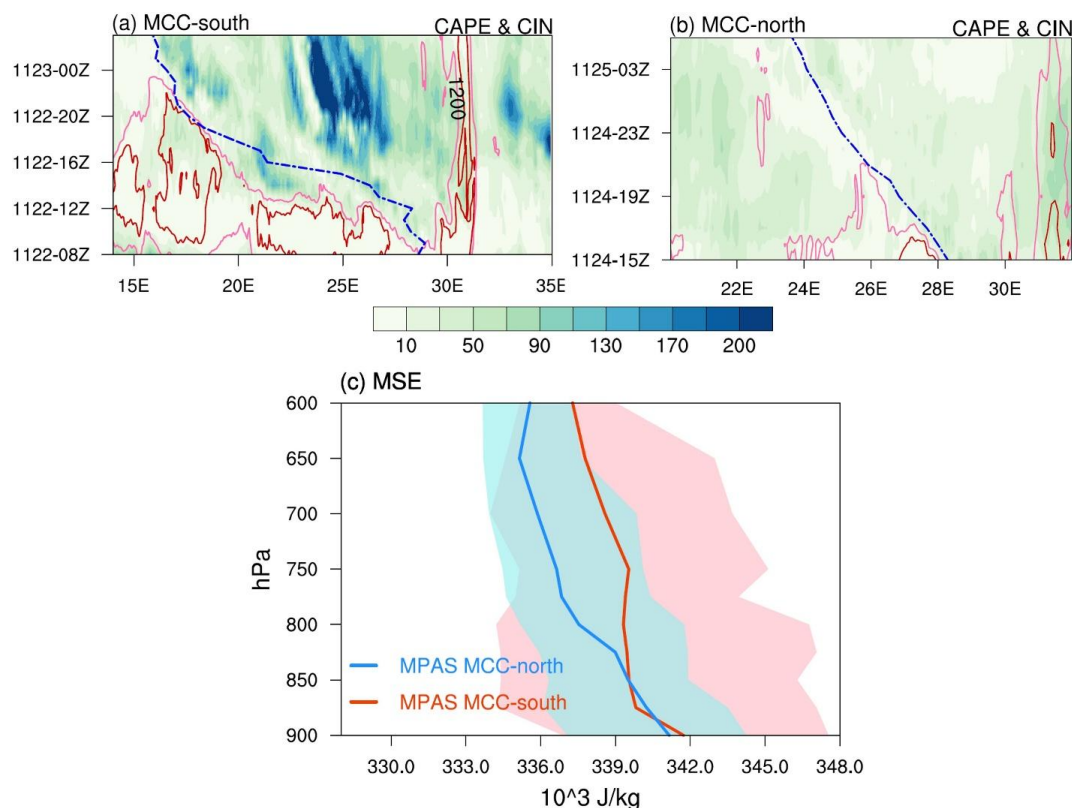
335 **Figure 6.** (a–c) Same as Figure 4, but for MCC-north from MPAS-A simulations. (d–e) Same as  
 336 Figure 5, but for 1.5°N–2.5°N averaged fields for MCC-north.

337

338 Figure 7a–b shows convective available potential energy (CAPE), which reflects  
 339 atmospheric instability and the potential for convection, and convective inhibition (CIN), which  
 340 represents the energy barrier that must be overcome for convection to initiate, for the two MCC  
 341 cases. For MCC-south, large CAPE values, as high as 2000 J/kg, consistently preceding the track  
 342 and accompanied by CIN values below 50 J/kg, create favorable conditions for convection  
 343 development. For MCC-north, CAPE is significantly lower, with CAPE values dropping below  
 344 1200 J/kg, and CIN also increases, during the mid-stage (around 21Z). In addition, we examine  
 345 the vertical profile of atmospheric energy. Following Hobbs & Wallace (2006), moist static energy  
 346 (MSE), which represents total energy of an air parcel, is expressed as:

$$MSE = L_v q + c_p T + \Phi, \quad (1)$$

347 where  $L_v$  is latent heat of vaporization,  $q$  is specific humidity,  $c_p$  is specific heat capacity at  
 348 constant pressure,  $T$  is air temperature, and  $\Phi$  is geopotential. Figure 7c shows that MSE decreases  
 349 with height for both MCC cases, indicating a convectively unstable environment favorable for  
 350 MCC developments. MCC-south exhibits higher MSE from 850 hPa to the mid-troposphere,  
 351 suggesting greater potential for convection and stronger moist updrafts.



352

353 **Figure 7.** (a) Hovmöller diagram for  $8^{\circ}\text{S}$ – $9^{\circ}\text{S}$  averaged CAPE (contours; J/kg; the light and dark  
 354 red contours represent 1200 J/kg and 2000 J/kg, respectively) and CIN (shading; J/kg) for MCC-  
 355 south from MPAS-A simulations. The blue dashed line represents the MCC track. (b) Same as (a),  
 356 but for  $1.5^{\circ}\text{N}$ – $2.5^{\circ}\text{N}$  averaged fields for MCC-north. (c) The mean MSE ( $10^3$  J/kg) for all timesteps  
 357 along the track of MCC-north (blue line) and MCC-south (red line) from MPAS-A simulations.  
 358 Shading represents the spread of the minimum and maximum values of MSE for all timesteps  
 359 along the track.

360

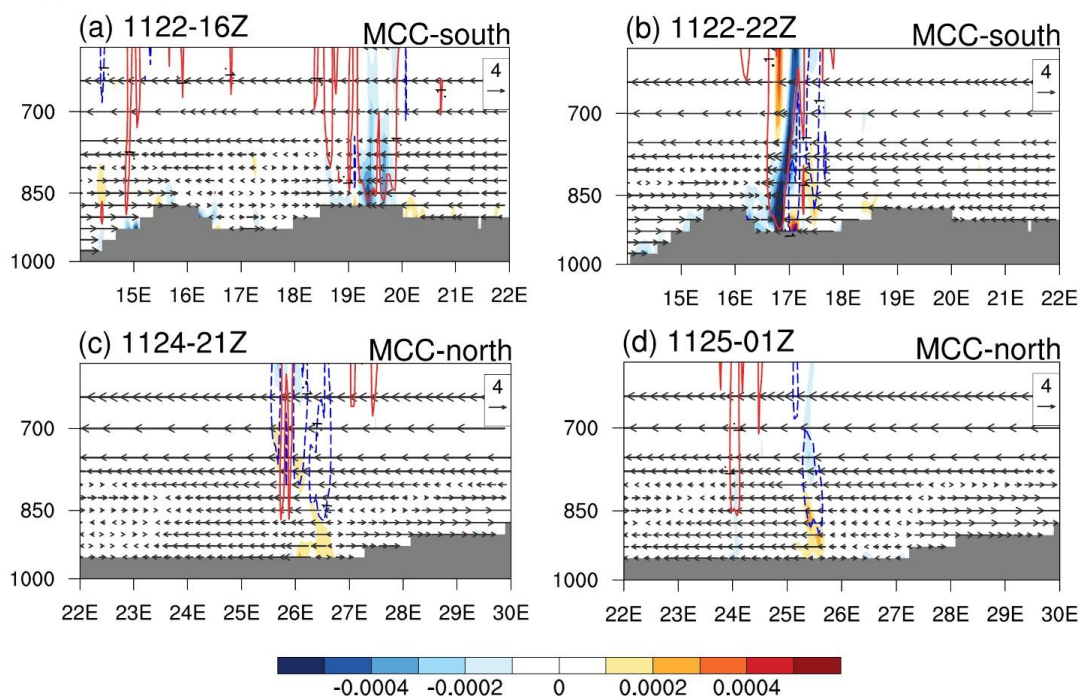
### 361 3.3 The role of vertical wind shear and AEJ

362 In this section, we examine dynamic factors driving the different evolutions of the two MCC  
 363 cases. Although previous studies have explored the relationship between MCSs over the Congo  
 364 Basin or equatorial Africa and dynamic factors such as vertical wind shear and AEJ (Nguyen &  
 365 Duvel, 2008; Jackson et al., 2009; Laing et al., 2011), they primarily relied on low-resolution  
 366 reanalysis data from a climate perspective without quantitative analyses based on MCS tracks.  
 367 Weather-focused investigations, such as quantifying the influence of these dynamic factors on  
 368 MCS developments along its track, require cloud-resolving model simulations (Laing et al., 2011).

369 During the mid-stage (16Z) of MCC-south, its convection, linked to low-tropospheric  
 370 convergence (blue shading) and updrafts (red contours), is concentrated over elevated terrain (Fig.

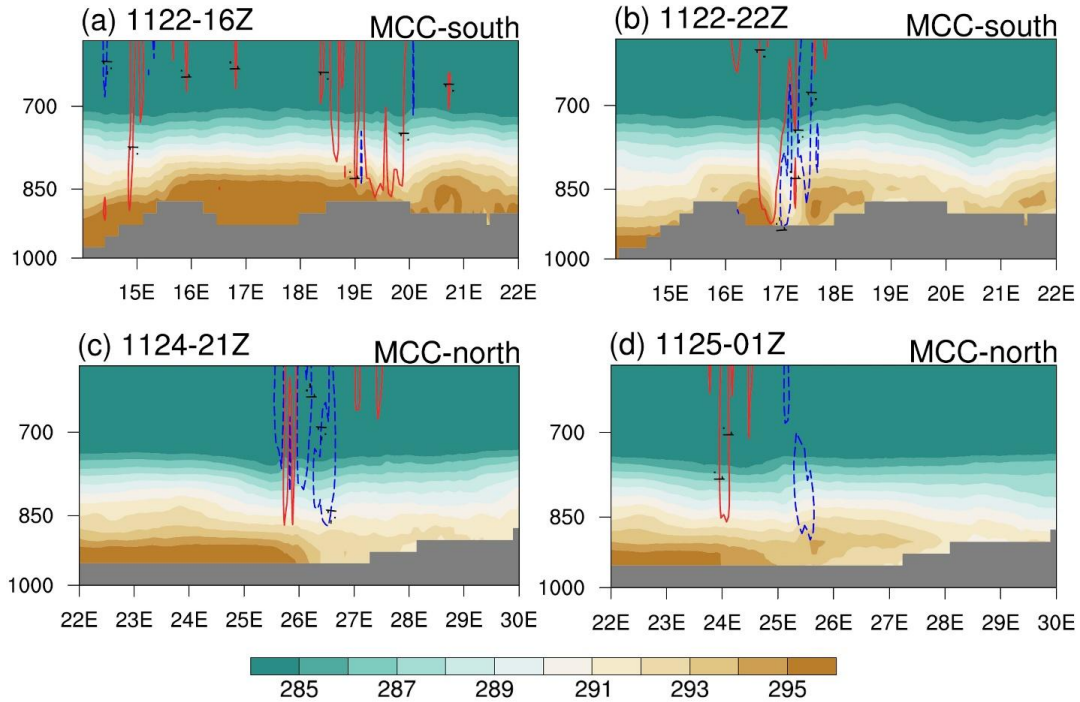


371 8a), with a cold pool region behind it (Fig. 9a). Westerly mountain-valley breezes ahead of the  
 372 MCC lift moisture-rich air from the lower troposphere, providing abundant latent energy to fuel  
 373 the system. As the MCC propagates into the valley, convergence intensifies from the surface to  
 374 the mid-troposphere, accompanied by enhanced vertical wind shear between the lower and mid-  
 375 troposphere ahead of the center (Fig. 8b) and a narrow cold pool region trailing the MCC center  
 376 (Fig. 9b). The vertical wind shear ahead of the MCC-south track is generally easterly. For MCC-  
 377 north, however, the system reaches the lowland forest region during its mid-stage (21Z), where  
 378 the lower troposphere is dominated by divergence (orange shading), inhibiting the upward  
 379 transport of low-level moisture to the mid-troposphere (Fig. 8c). The cold pool behind the MCC  
 380 center extends broadly in the zonal direction (from 26°E to 29°E, ~300 km), with temperatures  
 381 dropping by up to 4 K (291 K vs 295 K) (Fig. 9c).



382

383 **Figure 8.** (a–b) The 8°S–9°S averaged zonal (vectors; m/s) and vertical (contours; m/s; contour  
 384 values: –0.1 and 0.1 m/s) velocities and horizontal divergence (shading; s<sup>-1</sup>) for MCC-south from  
 385 MPAS-A simulations. (c–d), Same as (a–b), but for 1.5°N–2.5°N averaged fields for MCC-north.



386

387 **Figure 9.** (a–d) Same as Figure 8, but for air temperature (shading; K) and vertical velocity  
 388 (contours; m/s; contour values: –0.1 and 0.1 m/s).

389

390 Compared to MCC-south, lower-level westerly winds are absent ahead of the MCC-north,  
 391 resulting in generally weaker easterly wind shear (Fig. 8c–d); the cold pool is generally stronger  
 392 and extends broader zonally in MCC-north (Fig. 9c–d). According to Rotunno et al. (1988), that  
 393 is RKW theory, the weaker vertical wind shear may result from an overly strong cold pool,  
 394 characterized by greater intensity and broader horizontal extent in this case, causing the convective  
 395 system to tilt upshear and limiting MCC developments (e.g., Schumacher & Rasmussen, 2020;  
 396 Kirshbaum et al., 2025). In contrast, MCC-south features a more favorable balance between  
 397 vertical wind shear and cold pool strength, approaching the “optimal state” for MCC developments  
 398 during the mid-stage.

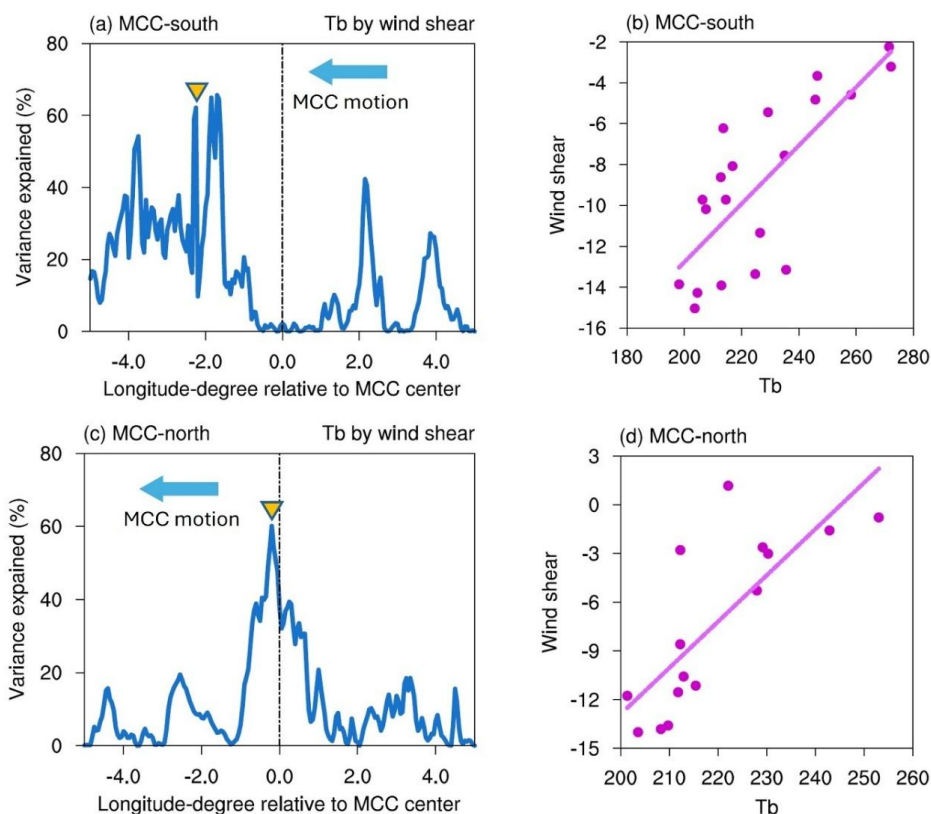
399 We further quantify how vertical wind shear influences MCC evolution by using a simple  
 400 linear regression model (e.g., Zhao & Fu, 2022):

$$Tb = \alpha + \beta \times \nabla U_x, \quad (2)$$

401 where  $Tb$  is brightness temperature at the MCC center,  $\nabla U_x$  is vertical zonal wind shear ( $U_{600} -$   
 402  $U_{875}$  for MCC-south and  $U_{600} - U_{900}$  for MCC-north) with the longitudinal distance ( $x$ ; i.e.,  
 403 degree) relative to the MCC center, and  $\alpha$  and  $\beta$  are regression coefficients. We calculate  
 404 coefficient of determination ( $R^2 = 1 - RSS/TSS$ , where  $RSS$  is sum of squares of residuals and  
 405  $TSS$  is total sum of squares) to assess how much of the variance in  $Tb$  can be explained by wind  
 406 shear.



407 Figure 10a shows that vertical wind shear located approximately 1.5° to 4° ahead of the  
 408 MCC-south center explains between 35% and 65% of the total variance in Tb, with the largest  
 409 explained variance around 2° west of the MCC center. This result suggests that vertical wind shear  
 410 ahead of the MCC-south center plays a key role in modulating convection, explaining up to 65%  
 411 of the Tb variance, and that this favorable environment may promote the formation of a gust front  
 412 ahead of the MCC center (Schumacher & Rasmussen, 2020). Strong convection (Tb < 220 K) is  
 413 associated with easterly wind shear exceeding 10 m/s (Fig. 10b). In contrast, for MCC-north, the  
 414 wind shear that significantly explains Tb variance (~60%) is confined near the center of the MCC,  
 415 with a sharp decline beyond 1° west of the center (Fig. 10c), indicating that the generation of  
 416 convective cells is primarily close to cold pool. During several timesteps along the track, MCC-  
 417 north exhibits weak or even westerly shear (positive values), despite persistent easterly flow in the  
 418 mid-troposphere along the MCC track (Fig. 10d). This suggests that the lower troposphere  
 419 experiences relatively stronger easterly winds than the mid-level.



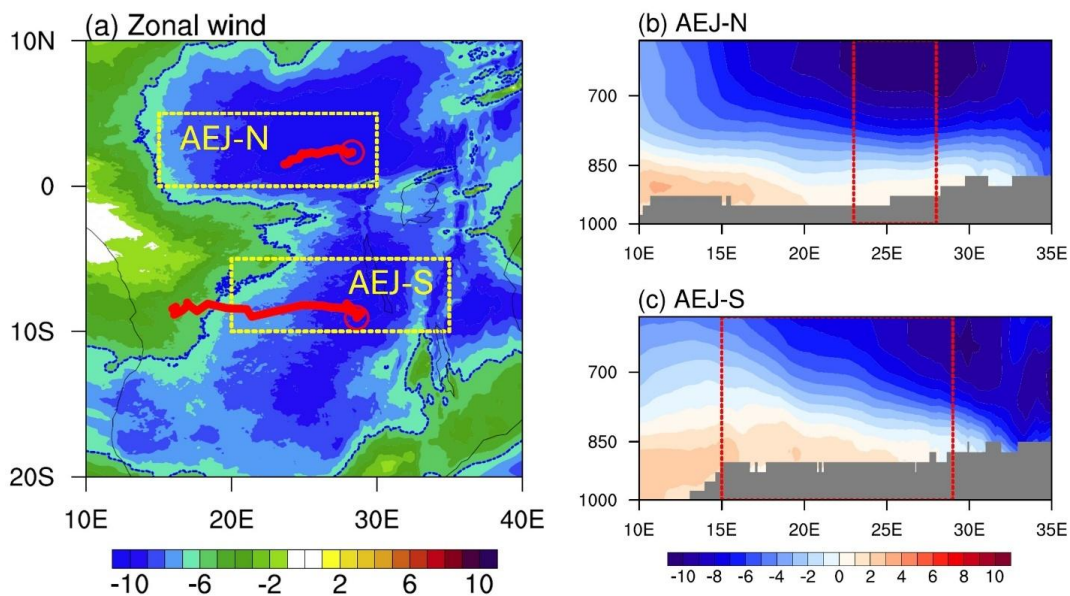
420  
 421 **Figure 10.** (a) Percentage of variance (i.e.,  $R^2 \times 100\%$ ) in Tb along the MCC-south track that can  
 422 be explained by vertical wind shear, shown as a function of longitude ahead and behind the MCC-  
 423 south track center. The yellow triangle indicates the longitude used in (b). (b) The scatter plot for  
 424 Tb (K) and wind shear (m/s) at the longitude ahead of MCC-south track (marked by the triangle  
 425 in (a)) for all timesteps along the track. The solid line represents the linear fit. (c–d) Same as (a–  
 426 b), but for MCC-north.



427

428 Therefore, compared to MCC-north, the longer duration and longer track of MCC-south  
429 are likely associated with a more favorable pre-existing wind shear structure extending up to ~400  
430 km ahead of the system. According to the RKW theory, this shear environment can achieve an  
431 “optimal” balance with the cold pool, effectively interacting with its outflow to lift warm, moist  
432 air, sustain updrafts, and promote the continued development and forward propagation of the  
433 MCC. These differences between the two MCC cases highlight the role of latitude and topography  
434 in modulating the impacts of environmental factors on MCS developments.

435 Finally, we investigate the linkage between the AEJ and the vertical wind shear associated  
436 with the two MCC cases. The AEJ system, consisting of both a northern and a southern branch  
437 (AEJ-N and AEJ-S), can promote mid-tropospheric moisture convergence within the right  
438 entrance region of the jet, thereby enhancing rainfall (Uccellini and Johnson, 1979; Jackson et al.,  
439 2009). Figure 11a shows zonal winds at 650 hPa averaged over the study period. The AEJ centers  
440 are typically identified by zonal wind speeds exceeding 6 m/s, and their approximate locations in  
441 this figure are consistent with previous studies (e.g., Jackson et al., 2009). MCC-north and MCC-  
442 south are located near the AEJ-N and AEJ-S, respectively. We define AEJ-N and AEJ-S indices  
443 as the domain-averaged zonal winds within the yellow boxes and calculate their correlations with  
444 vertical wind shear along MCC tracks. The strength of AEJ-N and AEJ-S is strongly positively  
445 correlated (correlation > 0.7) with the vertical shear associated with MCC-north and MCC-south,  
446 respectively (not shown). This suggests that the AEJ helps establish the wind shear conditions  
447 necessary for MCC developments. This is consistent with previous studies emphasizing the AEJ’s  
448 role in shear propagation over the West African monsoon region (Núñez Ocasio et al., 2020a).  
449 However, AEJ-N is notably stronger than AEJ-S (Fig. 11b vs 11c) and is associated with weaker  
450 low-level westerlies (lighter pink shading), which may lead to overall weaker convection in MCC-  
451 north.



452



453 **Figure 11.** (a) Zonal winds at 650 hPa (shading; m/s) averaged over November 21–25, 2023, from  
454 MPAS-A simulations. The blue contours (–6 m/s) indicate the typical threshold used to define the  
455 AEJ. The two yellow boxes represent the approximate locations of the AEJ-N and AEJ-S. The red  
456 lines represent the full tracks of the two MCC cases, and the open circles denote their initiation  
457 locations. (b–c) The 0°–5°N and 5°S–10°S averaged zonal wind (m/s) averaged over November  
458 21–25, 2023. The red boxes indicate the spatial extent during the lifespans of the two MCC cases.

459

#### 460 **4 Summary and discussion**

461 This study investigates mesoscale convective processes over the Congo Basin using  
462 MPAS-A. MCSs are objectively identified, tracked, and classified using the TAMS algorithm for  
463 the period of November 21–25, 2023, during which severe flooding was observed across the  
464 region. The model captures key MCS characteristics, including their general westward propagation  
465 and typical lifespans, although it overestimates rainfall—an issue attributed to known model biases  
466 (e.g., Raghavendra et al., 2022; Feng et al., 2023b, 2025). Among the identified MCSs, one long-  
467 lived and long-track MCC is well represented in terms of its timing and location, demonstrating  
468 the model’s capability to simulate MCC in the Congo Basin.

469 Two MCC cases—one over the southern mountainous region (MCC-south) and the other  
470 over the northern lowland forests (MCC-north)—are compared to examine the distinct  
471 environmental factors influencing MCC developments. Overall, MCC-south is larger in size,  
472 longer in duration, and moves over a longer distance than MCC-north. These differences are  
473 accompanied by higher CAPE and greater low- to mid-level MSE in MCC-south. The contrasting  
474 behavior is particularly evident during the mid-stage of each system: MCC-south shows enhanced  
475 convection associated with strong lower- to mid-level convergence and sustained updrafts,  
476 whereas MCC-north exhibits decreased convection, linked to low-level divergence. These  
477 differences reflect the role of vertical wind shear in MCC developments and its potential balance  
478 with the cold pool. MCC-south is associated with a more favorable pre-existing shear structure  
479 extending up to ~400 km ahead of the system, which explains up to 65% of the Tb variance, along  
480 with a moderate cold pool that provides a supportive environment for MCC developments  
481 according to RKW theory. In contrast, MCC-north is primarily influenced by wind shear near the  
482 system center and a stronger cold pool characterized by a temperature drop of up to 4 K and a  
483 zonal extent of ~300 km, both of which may inhibit MCC developments. Finally, while AEJ  
484 supports favorable shear (correlation > 0.7), an intensified jet may suppress low-level westerlies  
485 and weaken convection.

486 Compared to previous studies that examined the relationship between Congo Basin MCSs  
487 and environmental factors without quantitative investigations based on MCS tracks (e.g., Laing &  
488 Fritsch, 1993; Nguyen & Duvel, 2008; Jackson et al., 2009; Laing et al., 2011; Hartman, 2020;  
489 Mba et al., 2022; Nicholson, 2022; Kigotsi et al., 2022; Solimine et al., 2022; Andrews et al.,  
490 2024), this study provides a process-level view of the initiation, development, and propagation of  
491 MCSs in relation to environmental conditions closely tied to MCS tracks, underscoring the  
492 importance of convection-permitting simulations. In contrast to Raghavendra et al. (2022), who  
493 employed WRF to study MCSs in the Congo Basin, this study objectively identifies, tracks, and  
494 classifies MCSs using an automated algorithm, ensuring all analyses are based on well-captured  
495 MCS tracks. Furthermore, the roles of vertical wind shear and the AEJ in MCS developments are  
496 explicitly quantified.



497            This study has demonstrated the capability of MPAS-A in addressing a major knowledge  
498 gap in understanding MCSs and associated rainfall over the Congo Basin, an important region for  
499 global terrestrial water and ecosystems, where populations are among the most vulnerable  
500 globally. As a follow-up of this study, we will explicitly examine the influence of large-scale  
501 atmospheric dynamic fields and land surface conditions (especially the role of land–atmosphere  
502 interaction) on MCSs over the Congo Basin through numerical experiments by MPAS-A (e.g.,  
503 Koster et al., 2004; Imamovic et al., 2017; Núñez Ocasio et al., 2024). The insights gained have  
504 the potential to inform broader applications in other regions, particularly those lacking dense gauge  
505 networks. Ultimately, this work advocates for the use of state-of-the-art global cloud-resolving  
506 models to advance our understanding of MCSs, given their significant role in driving weather  
507 extremes and associated hazards with direct implications for socio-economic stability and human  
508 well-being.



509 **Code and data availability.** All the data used in this study are freely available online. The links  
510 to the data are provided in the reference. The MPAS version 8 modified to output isobaric variables  
511 is in <https://github.com/knubez>. The latest version of TAMS is in  
512 <https://zenodo.org/records/15353123>. The code and MPAS's outputs have been uploaded in  
513 <https://zenodo.org/records/15758254>.

514

515 **Author contributions.** SZ designed and performed observational analyses and model experiments  
516 and prepared the manuscript. RF designed the concepts and analyses of the manuscript. KNO, RN,  
517 CH, and JZ provide feedback and advice on MCS tracking, model experimental designs, and  
518 technical issues. All the authors revised the manuscript and provided helpful comments.

519

520 **Competing interests.** The authors have no competing interests to declare.

521

522 **Acknowledgments.** This study is mainly supported by the U.S. National Science Foundation  
523 (Award AGS-2404970 and AGS-1917781). Computing and data storage resources, including the  
524 Derecho supercomputer, were provided by the Computational and Information Systems Lab  
525 (CISL) at the National Center for Atmospheric Research (NCAR).

526

527 **Financial Support.** SZ and RF are supported by the U.S. National Science Foundation (Award  
528 Number AGS-1917781 and AGS-2404970).



529 **References**

- 530 Aloysius, N. R., Sheffield, J., Sainers, J. E., Li, H., & Wood, E. F.: Evaluation of historical and  
531 future simulations of precipitation and temperature in central Africa from CMIP5 climate  
532 models. *Journal Geophysical Research: Atmospheres*, 121, 130–152.  
533 <https://doi.org/10.1002/2015JD023656>, 2016.
- 534 Andrews, P.C., Cook, K.H. & Vizzy, E.K.: Mesoscale convective systems in the Congo Basin:  
535 seasonality, regionality, and diurnal cycles. *Climate Dynamics*, 62, 609–630.  
536 <https://doi.org/10.1007/s00382-023-06903-7>, 2024.
- 537 Baidu, M., Schwendike, J., Marsham, J. H., & Bain, C.: Effects of vertical wind shear on intensities  
538 of mesoscale convective systems over West and Central Africa. *Atmospheric Science*  
539 *Letters*, 23(8), e1094. <https://doi.org/10.1002/asl.1094>, 2022.
- 540 Barnes, H. C., & Houze, R. A.: The precipitating cloud population of the Madden-Julian  
541 Oscillation over the Indian and west Pacific Oceans. *Journal of Geophysical Research:*  
542 *Atmospheres*, 118, 6996–7023. <https://doi.org/10.1002/jgrd.50375>, 2013.
- 543 Brummett, R., Tanania, C., Pandi A., Ladel J., Munzini Y., ussell A.: Ressources en eau et biens  
544 et services liés à l'écosystème forestier. In: Wasseige, C., Devers, D., de Marcen, P., Eba'a  
545 Atyi, R., Nasi, R., & Mayaux, P. (Eds.) *Les forêts du Bassin du Congo*. Office des  
546 publications de l'Union européenne, Luxembourg. doi: 10.2788/32456, 2009.
- 547 Chakraborty, S., Fu, R., Wright, J. S., & Massie, S. T.: Relationships between convective structure  
548 and transport of aerosols to the upper troposphere deduced from satellite observations.  
549 *Journal of Geophysical Research: Atmospheres*, 120, 6515–6536.  
550 <https://doi.org/10.1002/2015JD023528>, 2015.
- 551 Chakraborty, S., Sullivan, S.C. and Feng, Z.: An Overview of Mesoscale Convective Systems:  
552 Global Climatology, Satellite Observations, and Modeling Strategies. In *Clouds and Their*  
553 *Climatic Impacts* (eds S.C. Sullivan and C. Hoose).  
554 <https://doi.org/10.1002/9781119700357.ch9>, 2023.
- 555 Chen, M., Shi, W., Xie, P., Silva, V. B. S., Kousky, V. E., & Higgins, R. W.: Assessing objective  
556 techniques for gauge-based analyses of global daily precipitation. *Journal of Geophysical*  
557 *Research Atmospheres*, 113(D4). <https://doi.org/10.1029/2007JD009132>, 2008.
- 558 Chen, X., Leung, L. R., Feng, Z., & Song, F.: Crucial Role of Mesoscale Convective Systems in  
559 the Vertical Mass, Water, and Energy Transports of the South Asian Summer Monsoon.  
560 *Journal of Climate*, 35(1), 91-108. <https://doi.org/10.1175/JCLI-D-21-0124.1>, 2022.
- 561 Chen, X., Leung, L. R., Feng, Z., & Yang, Q.: Environmental controls on MCS lifetime rainfall  
562 over tropical oceans. *Geophysical Research Letters*, 50, e2023GL103267.  
563 <https://doi.org/10.1029/2023GL103267>, 2023.
- 564 CICOS: Cahiers des statistiques sur les incidents et accidents et sur les flux de marchandises de  
565 2011–2012. [https://www.cicos.int/actualites/flux-des-marchandises-et-accidents-fluviaux-](https://www.cicos.int/actualites/flux-des-marchandises-et-accidents-fluviaux-dans-lespace-cicos-vers-des-statistiques-plus-fiables/)  
566 [dans-lespace-cicos-vers-des-statistiques-plus-fiables/](https://www.cicos.int/actualites/flux-des-marchandises-et-accidents-fluviaux-dans-lespace-cicos-vers-des-statistiques-plus-fiables/), 2012.
- 567 Clavner, M., Cotton, W. R., van den Heever, S. C., Saleeby, S. M., & Pierce, J. R.: The response  
568 of a simulated mesoscale convective system to increased aerosol pollution: Part I:



- 569           Precipitation intensity, distribution, and efficiency. *Atmospheric Research*, 199, 193–208.  
570           <https://doi.org/10.1016/j.atmosres.2017.08.010>, 2018.
- 571   Creese, A. and Washington, R.: Using qflux to constrain modeled Congo Basin rainfall in the  
572   CMIP5 ensemble. *Journal of Geophysical Research: Atmospheres*, 121(22), 13415–13442.  
573   <https://doi.org/10.1002/2016jd025596>, 2016.
- 574   Creese, A. & Washington, R.: A process-based assessment of CMIP5 rainfall in The Congo Basin:  
575   the September–November rainy season. *Journal of Climate*, 31, 7417–7439.  
576   <https://doi.org/10.1175/JCLI-D-17-0818.1>, 2018.
- 577   Creese, A., Washington, R., & Munday, C.: The plausibility of September–October–November  
578   Congo Basin rainfall change in coupled climate models. *Journal of Geophysical Research:*  
579   *Atmospheres*, 124, 5822–5846. <https://doi.org/10.1029/2018JD029847>, 2019.
- 580   Davies, R.: Flooding in the Democratic Republic of the Congo and Congo-Brazzaville, January  
581   2024. Copernicus. [https://global-flood.emergency.copernicus.eu/news/159-flooding-in-](https://global-flood.emergency.copernicus.eu/news/159-flooding-in-the-democratic-republic-of-the-congo-and-congo-brazzaville-january-2024/)  
582   [the-democratic-republic-of-the-congo-and-congo-brazzaville-january-2024/](https://global-flood.emergency.copernicus.eu/news/159-flooding-in-the-democratic-republic-of-the-congo-and-congo-brazzaville-january-2024/), 2024.
- 583   Dyer, E. L. E., Jones, D. B. A., Nusbaumer, J., Li, H., Collins, O., Vettoretti, G., & Noone, D.:  
584   Congo Basin precipitation: Assessing seasonality, regional interactions, and sources of  
585   moisture. *Journal of Geophysical Research: Atmospheres*, 122(13), 6882–6898.  
586   <https://doi.org/10.1002/2016JD026240>, 2017.
- 587   Evans, J. L., & Shemo, R. E.: A Procedure for Automated Satellite-Based Identification and  
588   Climatology Development of Various Classes of Organized Convection. *Journal of*  
589   *Applied Meteorology and Climatology*, 35(5), 638–652. [https://doi.org/10.1175/1520-](https://doi.org/10.1175/1520-0450(1996)035<0638:APFASB>2.0.CO;2)  
590   [0450\(1996\)035<0638:APFASB>2.0.CO;2](https://doi.org/10.1175/1520-0450(1996)035<0638:APFASB>2.0.CO;2), 1996.
- 591   Feng, Z., Houze, R. A., Jr., Leung, L. R., Song, F., Hardin, J. C., Wang, J., Gustafson, W. I., Jr.,  
592   & Homeyer, C. R.: Spatiotemporal Characteristics and Large-Scale Environments of  
593   Mesoscale Convective Systems East of the Rocky Mountains. *Journal of Climate*, 32(21),  
594   7303–7328. <https://doi.org/10.1175/JCLI-D-19-0137.1>, 2019.
- 595   Feng, Z., Leung, L. R., Liu, N., Wang, J., Houze, R. A., Li, J., et al.: A global high-resolution  
596   mesoscale convective system database using satellite-derived cloud tops, surface  
597   precipitation, and tracking. *Journal of Geophysical Research: Atmospheres*, 126(8).  
598   <https://doi.org/10.1029/2020JD034202>, 2021.
- 599   Feng, Z., Leung, L. R., Hardin, J., Terai, C. R., Song, F., & Caldwell, P.: Mesoscale convective  
600   systems in DYAMOND global convection-permitting simulations. *Geophysical Research*  
601   *Letters*, 50(4), e2022GL102603. <https://doi.org/10.1029/2022gl102603>, 2023a.
- 602   Feng, Z., Hardin, J., Barnes, H. C., Li, J., Leung, L. R., Varble, A., & Zhang, Z.: PyFLEXTRKR:  
603   A flexible feature tracking Python software for convective cloud analysis. *Geoscientific*  
604   *Model Development*, 16(10), 2753–2776. <https://doi.org/10.5194/gmd-16-2753-2023>,  
605   2023b.
- 606   Feng, Z., Prein, A. F., Kukulies, J., Fiolleau, T., Jones, W. K., Maybee, B., et al.: Mesoscale  
607   convective systems tracking method intercomparison (MCSMIP): Application to



- 608 DYAMOND global km-scale simulations. *Journal of Geophysical Research:*  
609 *Atmospheres*, 130, e2024JD042204. <https://doi.org/10.1029/2024JD042204>, 2025.
- 610 Fotso-Kamga, G., Fotso-Nguemo, T. C., Diallo, I., Yepdo, Z. D., Pokam, W. M., Vondou, D. A.,  
611 & Lenouo, A.: An evaluation of COSMO-CLM regional climate model in simulating  
612 precipitation over Central Africa. *International Journal of Climatology*, 40(5), 2891–2912.  
613 <https://doi.org/10.1002/joc.6372>, 2020.
- 614 Hamilton, H. L., G. S. Young, J. L. Evans, J. D. Fuentes, and K. M. Núñez Ocasio: The  
615 relationship between the Guinea Highlands and the West African offshore rainfall  
616 maximum, *Geophys. Res. Lett.*, 44, 1158–1166, doi:10.1002/2016GL071170, 2017.
- 617 Hamilton, H. L., Núñez Ocasio, K. M., Evans, J. L., Young, G. S., & Fuentes, J. D.: Topographic  
618 influence on the African Easterly Jet and African Easterly Wave energetics. *Journal of*  
619 *Geophysical Research: Atmospheres*, 125,  
620 e2019JD032138. <https://doi.org/10.1029/2019JD032138>, 2020.
- 621 Hartman, A.T.: Tracking mesoscale convective systems in central equatorial Africa. *International*  
622 *Journal of Climatology*, 41(1), 469–482. <https://doi.org/10.1002/joc.6632>, 2020.
- 623 Hersbach, H., Bell, B., Berrisford, P., Hirahara, S., Horányi, A., Muñoz-Sabater, J., et al.: The  
624 ERA5 global reanalysis. *Quarterly Journal of the Royal Meteorological Society*, 146(730),  
625 1999–2049. <https://doi.org/10.1002/qj.3803>, 2020.
- 626 Hobbs, P. V., and J. M. Wallace: *Atmospheric Science: An Introductory Survey*. 2nd ed. Academic  
627 Press, 86pp, 2006.
- 628 Hong, S. Y., & Lim, J.: The WRF single-moment 6-class microphysics scheme (WSM6). *Journal*  
629 *of the Korean Meteorological Society*, 42, 129–151, 2006.
- 630 Hong, S., Noh, Y., & Dudhia, J.: A New Vertical Diffusion Package with an Explicit Treatment  
631 of Entrainment Processes. *Monthly Weather Review*, 134(9), 2318–2341.  
632 <https://doi.org/10.1175/MWR3199.1>, 2006.
- 633 Hopsch, S. B., Thorncroft, C. D., & Tyle, K. R.: Analysis of African Easterly Wave Structures and  
634 Their Role in Influencing Tropical Cyclogenesis. *Monthly Weather Review*, 138(4), 1399–  
635 1419. <https://doi.org/10.1175/2009MWR2760.1>, 2010.
- 636 Houze, R. A.: Mesoscale convective systems. *Reviews of Geophysics*, 42(4), RG4003.  
637 <http://dx.doi.org/10.1029/2004RG000150>, 2004.
- 638 Houze, R. A.: 100 years of research on mesoscale convective systems. *Meteorological*  
639 *Monographs*, 59, 17.1–17.54. <https://doi.org/10.1175/amsmonographs-d-18-0001.1>, 2018.
- 640 Huffman, G.J., E.F. Stocker, D.T. Bolvin, E.J. Nelkin, J. Tan.: GPM IMERG Final Precipitation  
641 L3 Half Hourly 0.1 degree x 0.1 degree V07, Greenbelt, MD, Goddard Earth Sciences Data  
642 and Information Services Center (GES DISC), 10.5067/GPM/IMERG/3B-HH/07, 2023.
- 643 Hughes, D. A.: Comparison of satellite rainfall data with observations from gauging station  
644 networks. *Journal of Hydrology*, 327(3–4), 399–410.  
645 <https://doi.org/10.1016/j.jhydrol.2005.11.041>, 2006.



- 646 Iacono, M. J., Delamere, J. S., Mlawer, E. J., Shephard, M. W., Clough, S. A., & Collins, W. D.:  
647 Radiative forcing by long-lived greenhouse gases: Calculations with the AER radiative  
648 transfer models. *Journal of Geophysical Research*, 113(D13), D13103.  
649 <https://doi.org/10.1029/2008JD009944>, 2008.
- 650 Imamovic, A., Schlemmer, L., & Schär, C.: Collective impacts of orography and soil moisture on  
651 the soil moisture-precipitation feedback. *Geophysical Research Letters*, 44, 11,682–  
652 11,691. <https://doi.org/10.1002/2017GL075657>, 2017
- 653 Jackson, B., Nicholson, S. E., & Klotter, D.: Mesoscale Convective Systems over Western  
654 Equatorial Africa and Their Relationship to Large-Scale Circulation. *Monthly Weather*  
655 *Review*, 137(4), 1272-1294. <https://doi.org/10.1175/2008MWR2525.1>, 2009.
- 656 Janowiak J., Bob Joyce, Pingping Xie.: NCEP/CPC L3 Half Hourly 4km Global (60S - 60N)  
657 Merged IR V1, Edited by Andrey Savtchenko, Greenbelt, MD, Goddard Earth Sciences  
658 Data and Information Services Center (GES DISC) [Dataset]. 10.5067/P4HZB9N27EKU,  
659 2017.
- 660 Jiménez, P. A., Dudhia, J., González-Rouco, J. F., Navarro, J., Montávez, J. P., & García-  
661 Bustamante, E.: A Revised Scheme for the WRF Surface Layer Formulation. *Monthly*  
662 *Weather Review*, 140(3), 898-918. <https://doi.org/10.1175/MWR-D-11-00056.1>, 2012.
- 663 Joachim, E.I., Vanel, A.R., & Youssif, G.T.: Climate Change and Urban Risks: Understanding and  
664 Analysing the Vulnerability of the City Of Brazzaville in the Republic Of Congo to  
665 Flooding in 2023. *Pakistan Journal of Life and Social Sciences*, 22(2): 8907-8918.  
666 <https://doi.org/10.57239/PJLSS-2024-22.2.00673>, 2024.
- 667 Kigotsi, J.K., Soula, S., Kazadi, A.B.M., & Zana, A.N.: Contribution to the study of thunderstorms  
668 in the Congo Basin: Analysis of periods with intense activity. *Atmospheric Research*, 269,  
669 106013. doi: org/10.1016/j.atmosres.2021.106013, 2022.
- 670 Kirshbaum, D. J., Sindhu, K. D., & Turner, D. D.: An Observational Evaluation of RKW Theory  
671 over the U.S. Southern Great Plains. *Journal of the Atmospheric Sciences*, 82(7), 1341-  
672 1360. <https://doi.org/10.1175/JAS-D-24-0185.1>, 2025.
- 673 Koster, R. D., Dirmeyer, P., Guo, Z., Bonan, G., Chan, E., Cox, P., Gordon, C. T., Kanae, S.,  
674 Kowalczyk, E., Lawrence, D., Liu, P., Lu, C.-H., Malyshec, S., McAvaney, B., Mitchell,  
675 K., Mocko, D., Oki, T., Oleson, K., Pitman, A., Sud, Y. C., Taylor, C. M., Verseghy, D.,  
676 Vasic, R., Xue, Y., and Yamada, T.: Regions of Strong Coupling Between Soil Moisture  
677 and Precipitation, *Science*, 305, 1138–1140, <https://doi.org/10.1126/science.1100217>,  
678 2004.
- 679 Kunkel, K. E., Easterling, D. R., Kristovich, D. A. R., Gleason, B., Stoecker, L., & Smith, R.:  
680 Meteorological Causes of the Secular Variations in Observed Extreme Precipitation Events  
681 for the Conterminous United States. *Journal of Hydrometeorology*, 13(3), 1131-1141.  
682 <https://doi.org/10.1175/JHM-D-11-0108.1>, 2012.
- 683 Laing, A. G., and J. Fritsch, J. M.: Mesoscale Convective Complexes in Africa. *Monthly Weather*  
684 *Review*, 121.8, 2254-2263. [https://doi.org/10.1175/1520-0493\(1993\)121<2254:MCCIA>2.0.CO;2](https://doi.org/10.1175/1520-0493(1993)121<2254:MCCIA>2.0.CO;2), 1993.



- 686 Laing, A. G., & Fritsch, J. M.: The global population of mesoscale convective complexes.  
687 Quarterly Journal of the Royal Meteorological Society, 123(538), 389–405.  
688 <https://doi.org/10.1002/qj.49712353807>, 1997.
- 689 Laing, A. G., Carbone, R. E., & Levizzani, V. : Cycles and propagation of deep convection  
690 over equatorial Africa. Monthly Weather Review, 139(9), 2832–2853.  
691 doi:10.1175/2011mwr3500.1, 2011.
- 692 Lee, C., Cheung, K. K. W., Hui, J. S. N., & Elsberry, R. L.: Mesoscale Features Associated with  
693 Tropical Cyclone Formations in the Western North Pacific. Monthly Weather Review,  
694 136(6), 2006–2022. <https://doi.org/10.1175/2007MWR2267.1>, 2008.
- 695 Li, B., H. Beaudoin, and M. Rodell, NASA/GSFC/HSL: GLDAS Catchment Land Surface Model  
696 L4 daily 0.25 x 0.25 degree GRACE-DA1 V2.2, Greenbelt, Maryland, USA, Goddard  
697 Earth Sciences Data and Information Services Center (GES DISC) [Dataset].  
698 10.5067/TXBMLX370XX8, 2020.
- 699 Maddox, R. A.: Mesoscale convective complexes. Bulletin of the American Meteorological  
700 Society, 61(11), 1374–1400. [https://doi.org/10.1175/1520-0477\(1980\)061<1374:MCC>2.0.CO;2](https://doi.org/10.1175/1520-0477(1980)061<1374:MCC>2.0.CO;2), 1980.
- 702 Mayta, V. C., Adames Corraliza, Á. F., Torres Maldonado, K., Luo, H., & Núñez Ocasio, K. M.:  
703 Thermodynamic Processes Governing the Evolution of Developing and Strong  
704 Nondeveloping African Easterly Waves. Journal of the Atmospheric Sciences, 82(6),  
705 1161–1174. <https://doi.org/10.1175/JAS-D-24-0125.1>, 2025.
- 706 Mba, W.P., Vondou, D.A. and Kamsu-Tamo, P.H.: Central African Climate. In Congo Basin  
707 Hydrology, Climate, and Biogeochemistry (eds R.M. Tshimanga, G.D.M. N'kaya and D.  
708 Alsdorf). <https://doi.org/10.1002/9781119657002.ch2>, 2022.
- 709 Mohr, K. I., Famiglietti, J. S., & Zipser, E. J.: The contribution to tropical rainfall with respect to  
710 convective system type, size, and intensity estimated from the 85-GHz ice-scattering  
711 signature. Journal of Applied Meteorology, 38(5): 596–606. [https://doi.org/10.1175/1520-0450\(1999\)038<0596:TCTTRW>2.0.CO;2](https://doi.org/10.1175/1520-0450(1999)038<0596:TCTTRW>2.0.CO;2), 1999.
- 713 Muetzelfeldt, M. R., Plant, R. S., Christensen, H. M., Zhang, Z., Woollings, T., Feng, Z., & Li, P.:  
714 Environmental Conditions Affecting Global Mesoscale Convective System Occurrence.  
715 Journal of the Atmospheric Sciences, 82(2), 391–407. <https://doi.org/10.1175/JAS-D-24-0058.1>, 2025.
- 717 Nguyen, H. and Duvel, J.P.: Synoptic wave perturbations and convective systems over equatorial  
718 Africa. Journal of Climate, 21, 6372–6388. <https://doi.org/10.1175/2008JCLI2409.1>,  
719 2008.
- 720 Nicholson, S. E.: The ITCZ and the seasonal cycle over equatorial Africa. Bulletin of the American  
721 Meteorological Society, 99(2), 337–348. <https://doi.org/10.1175/BAMS-D-16-0287.1>,  
722 2018.
- 723 Nicholson, S. E., Klotter, D., Dezfuli, A. K., & Zhou, L.: New Rainfall Datasets for the Congo  
724 Basin and Surrounding Regions. Journal of Hydrometeorology, 19(8), 1379–1396.  
725 <https://doi.org/10.1175/JHM-D-18-0015.1>, 2018.



- 726 Nicholson, S. E.: The Rainfall and Convective Regime over Equatorial Africa, with Emphasis on  
727 the Congo Basin. 25–48. <https://doi.org/10.1002/9781119657002.CH3>, 2022.
- 728 Niu, G.-Y., Yang, Z.-L., Mitchell, K. E., Chen, F., Ek, M. B., Barlage, M., et al.: The community  
729 Noah land surface model with multiparameterization options (Noah-MP): 1. Model  
730 description and evaluation with local-scale measurements. *Journal of Geophysical*  
731 *Research*, 116(D12), D12109. <https://doi.org/10.1029/2010JD015139>, 2011.
- 732 N'kaya, G.D.M., Laraque, A., Paturel, J.-E., Guzanga, G.G., Mahé, G. and Tshimanga, R.M.: A  
733 New Look at Hydrology in the Congo Basin, Based on the Study of Multi-Decadal Time  
734 Series. In *Congo Basin Hydrology, Climate, and Biogeochemistry* (eds R.M. Tshimanga,  
735 G.D.M. N'kaya and D. Alsdorf). <https://doi.org/10.1002/9781119657002.ch8>, 2022.
- 736 Núñez Ocasio, K. M., Evans, J. L., & Young, G. S.: A wave-relative framework analysis of AEW–  
737 MCS interactions leading to tropical cyclogenesis. *Monthly Weather Review*, 148(11),  
738 4657–4671. <https://doi.org/10.1175/MWR-D-20-0152.1>, 2020a.
- 739 Núñez Ocasio, K. M., Evans, J. L., & Young, G. S.: Tracking Mesoscale Convective Systems that  
740 are Potential Candidates for Tropical Cyclogenesis. *Monthly Weather Review*, 148(2),  
741 655–669. <https://doi.org/10.1175/MWR-D-19-0070.1>, 2020b.
- 742 Núñez Ocasio, K. M., Brammer, A., Evans, J. L., Young, G. S., & Moon, Z. L.: Favorable monsoon  
743 environment over eastern Africa for subsequent tropical cyclogenesis of African easterly  
744 waves. *Journal of the Atmospheric Sciences*, 78(9), 2911–2925.  
745 <https://doi.org/10.1175/JAS-D-20-0339.1>, 2021.
- 746 Núñez Ocasio, K. M., & Rios-Berrios, R.: African easterly wave evolution and tropical  
747 cyclogenesis in a pre-Helene (2006) hindcast using the Model for Prediction Across Scales–  
748 Atmosphere (MPAS-A). *Journal of Advances in Modeling Earth Systems*, 15,  
749 e2022MS003181. <https://doi.org/10.1029/2022MS003181>, 2023.
- 750 Núñez Ocasio, K. M., & Dougherty, E. M.: The effect of pseudo-global warming on the weather-  
751 climate system of Africa in a convection-permitting model. *Geophysical Research Letters*,  
752 51, e2024GL112341. <https://doi.org/10.1029/2024GL112341>, 2024.
- 753 Núñez Ocasio, K. M., Davis, C. A., Moon, Z. L., & Lawton, Q. A.: Moisture dependence of an  
754 african easterly wave within the west african monsoon system. *Journal of Advances in*  
755 *Modeling Earth Systems*, 16(6), e2023MS004070.  
756 <https://doi.org/10.1029/2023MS004070>, 2024.
- 757 Núñez Ocasio, K. M., & Moon, Z. L.: TAMS: A tracking, classifying, and variable-assigning  
758 algorithm for mesoscale convective systems in simulated and satellite-derived datasets.  
759 *Geoscientific Model Development*, 17, 6035–6049. [https://doi.org/10.5194/gmd-17-6035-](https://doi.org/10.5194/gmd-17-6035-2024)  
760 [2024](https://doi.org/10.5194/gmd-17-6035-2024), 2024.
- 761 Peters, J. M., & Schumacher, R. S.: Dynamics governing a simulated mesoscale convective system  
762 with a training convective line. *Journal of the Atmospheric Sciences*, 73(7), 2643–2664.  
763 <https://doi.org/10.1175/JAS-D-15-0199.1>, 2016.



- 764 Pokam, W. M., Bain, C. L., Chadwick, R. S., Graham, R., Sonwa, D. J., & Kamga, F. M.:  
765 Identification of Processes Driving Low-Level Westerlies in West Equatorial Africa.  
766 *Journal of Climate*, 27(11), 4245-4262. <https://doi.org/10.1175/JCLI-D-13-00490.1>, 2014.
- 767 Prein, A. F., Feng, Z., Fiolleau, T., Moon, Z. L., Núñez Ocasio, K. M., Kukulies, J., et al.: Km-  
768 scale simulations of mesoscale convective systems over South America—A feature tracker  
769 intercomparison. *Journal of Geophysical Research: Atmospheres*, 129,  
770 e2023JD040254. <https://doi.org/10.1029/2023JD040254>, 2024.
- 771 Raghavendra, A., Xia, G., Zhou, L., & Jiang, Y.: Orographic enhancement of rainfall over the  
772 Congo Basin. *Atmospheric Science Letters*, 23(4), e1079. <https://doi.org/10.1002/asl.1079>,  
773 2022.
- 774 Rasmussen, K. L. , Chaplin, M. M. , Zuluaga, M. D. , & Houze , R. A. , Jr.: Contribution of  
775 Extreme Convective Storms to Rainfall in South America. *Journal of Hydrometeorology*,  
776 17(1), 353-367. <https://doi.org/10.1175/JHM-D-15-0067.1>, 2016.
- 777 Rehbein, A., Ambrizzi, T., Mechoso, C. R., Espinosa, S. A. I., & Myers, T. A.: Mesoscale  
778 convective systems over the Amazon basin: The GoAmazon2014/5 program. *International*  
779 *Journal of Climatology*, 39, 5599–5618. <https://doi.org/10.1002/joc.6173>, 2019.
- 780 Rotunno, R., Klemp, J. B., & Weisman, M. L.: A Theory for Strong, Long-Lived Squall Lines.  
781 *Journal of Atmospheric Sciences*, 45(3), 463-485. [https://doi.org/10.1175/1520-  
782 0469\(1988\)045<0463:ATFSSL>2.0.CO;2](https://doi.org/10.1175/1520-0469(1988)045<0463:ATFSSL>2.0.CO;2), 1988.
- 783 Satoh, M., Stevens, B., Judt, F., Khairoutdinov, M., Lin, S.-J., Putman, W. M., & Duben, P.: Global  
784 cloud-resolving models. *Current Climate Change Reports*, 5, 172–184.  
785 <https://doi.org/10.1007/s40641-019-00131-0>, 2019.
- 786 Schumacher, R. S., & Rasmussen, K. L.: The formation, character and changing nature of  
787 mesoscale convective systems. *Nature Reviews Earth & Environment*, 1(6), 300–314.  
788 <https://doi.org/10.1038/s43017-020-0057-7>, 2020.
- 789 Schumann, G.J.-P., Moller, D.K., Croneborg-Jones, L. and Andreadis, K.M.: Reviewing  
790 Applications of Remote Sensing Techniques to Hydrologic Research in Sub-Saharan  
791 Africa, with a Special Focus on the Congo Basin. In *Congo Basin Hydrology, Climate, and*  
792 *Biogeochemistry* (eds R.M. Tshimanga, G.D.M. N'kaya and D. Alsdorf).  
793 <https://doi.org/10.1002/9781119657002.ch16>, 2022.
- 794 Skamarock, W. C., Klemp, J. B., Duda, M. G., Fowler, L. D., Park, S., & Ringler, T. D.: A  
795 Multiscale Nonhydrostatic Atmospheric Model Using Centroidal Voronoi Tessellations and  
796 C-Grid Staggering. *Monthly Weather Review*, 140(9), 3090-3105.  
797 <https://doi.org/10.1175/MWR-D-11-00215.1>, 2012.
- 798 Smith, B. T., Thompson, R. L., Grams, J. S., Broyles, C., & Brooks, H. E.: Convective Modes for  
799 Significant Severe Thunderstorms in the Contiguous United States. Part I: Storm  
800 Classification and Climatology. *Weather and Forecasting*, 27(5), 1114-1135.  
801 <https://doi.org/10.1175/WAF-D-11-00115.1>, 2012.



- 802 Solimine, S.L., Zhou, L., Raghavendra, A., Cai, Y.: Relationships between intense convection,  
803 lightning, and rainfall over the interior Congo Basin using TRMM data, *Atmospheric*  
804 *Research*, 273, 106164. <https://doi.org/10.1016/j.atmosres.2022.106164>, 2022.
- 805 Stevens, B., Satoh, M., Auger, L., Biercamp, J., Bretherton, C. S., Chen, X., Düben, P., Judt, F.,  
806 Khairoutdinov, M., Klocke, D., Kodama, C., Kornbluh, L., Lin, S.-J., Neumann, P.,  
807 Putman, W. M., Röber, N., Shibuya, R., Vanniere, B., Vidale, P. L., Wedi, N., and Zhou,  
808 L.: DYAMOND: The DYnamics of the Atmospheric general circulation Modeled On Non-  
809 hydrostatic Domains, *Prog. Earth Planet. Sci.*, 6, 61, [https://doi.org/10.1186/s40645-019-](https://doi.org/10.1186/s40645-019-0304-z)  
810 0304-z, 2019.
- 811 Sullivan, S. C., Schiro, K. A., Stubenrauch, C., & Gentine, P.: The response of tropical organized  
812 convection to El Niño warming. *Journal of Geophysical Research: Atmospheres*, 124,  
813 8481–8500. <https://doi.org/10.1029/2019JD031026>, 2019.
- 814 Sultan, B., Janicot, S., & Diedhiou, A.: The West African monsoon dynamics. Part I:  
815 Documentation of intraseasonal variability. *Journal of Climate*, 16, 3389–3406.  
816 [https://doi.org/10.1175/1520-0442\(2003\)016<3389:TWAMDP>2.0.CO;2](https://doi.org/10.1175/1520-0442(2003)016<3389:TWAMDP>2.0.CO;2), 2003.
- 817 Trismidianto, Yulihastin, E., Satyawardhana, H., Nugroho, J.T., Ishida, S.: The contribution of the  
818 mesoscale convective complexes (MCCs) to total rainfall over Indonesian maritime  
819 continent the contribution of the mesoscale convective complexes (MCCs) to total rainfall  
820 over Indonesian maritime continent. *Earth and Environmental Science*, 54, 012027.  
821 <https://doi.org/10.1088/1742-6596/755/1/011001>, 2017.
- 822 Tsakrakilides, G., & Evans, J. L.: Global and Regional Diurnal Variations of Organized  
823 Convection. *Journal of Climate*, 16(10), 1562-1572. [https://doi.org/10.1175/1520-](https://doi.org/10.1175/1520-0442(2003)016<1562:GARDVO>2.0.CO;2)  
824 0442(2003)016<1562:GARDVO>2.0.CO;2, 2003.
- 825 Tshimanga, R.M., Tshitenge, J.M., Kabuya, P., Alsdorf, D., Mahe, G., Kibukusa, G., & Lukanda  
826 V.: A regional perspective of flood forecasting and disaster management systems for the  
827 Congo River Basin. In: T.E. Adams, & T. C Pagano. (Eds.), *Flood Forecasting: A Global*  
828 *Perspective*, ISBN: 978-0-12-801884-2, ELSEVIER, 2016.
- 829 Tshimanga, R.M., N'kaya, G.D.M., Laraque, A., Nicholson, S.E., Onema, J.-M.K., Lumbuenamo,  
830 R. and Alsdorf, D.: Congo Basin Research. In *Congo Basin Hydrology, Climate, and*  
831 *Biogeochemistry* (eds R.M. Tshimanga, G.D.M. N'kaya and D. Alsdorf).  
832 <https://doi.org/10.1002/9781119657002.ch1>, 2022.
- 833 Uccellini, L. W., & Johnson, D. R.: The Coupling of Upper and Lower Tropospheric Jet Streaks  
834 and Implications for the Development of Severe Convective Storms. *Monthly Weather*  
835 *Review*, 107(6), 682-703. [https://doi.org/10.1175/1520-](https://doi.org/10.1175/1520-0493(1979)107<0682:TCOUAL>2.0.CO;2)  
836 0493(1979)107<0682:TCOUAL>2.0.CO;2, 1979.
- 837 Wang, W.: Forecasting Convection with a “Scale-Aware” Tiedtke Cumulus Parameterization  
838 Scheme at Kilometer Scales. *Weather and Forecasting*, 37(8), 1491-1507.  
839 <https://doi.org/10.1175/WAF-D-21-0179.1>, 2022.
- 840 Washington, R., James, R., Pearce, H., Pokam, W. M., & Moufouma-Okia, W.: Congo basin  
841 rainfall climatology: Can we believe the climate models? *Philosophical Transactions of the*



- 842 Royal Society B: Biological Sciences, 368(1625). <https://doi.org/10.1098/rstb.2012.0296>,  
843 2013.
- 844 Xie, P., Joyce, R., Wu, S., Yoo, S.-H., Yarosh, Y., Sun, F., Lin, R., & NOAA CDR Program:  
845 NOAA Climate Data Record (CDR) of CPC Morphing Technique (CMORPH) High  
846 Resolution Global Precipitation Estimates, Version 1. NOAA National Centers for  
847 Environmental Information [Dataset]. <https://doi.org/10.25921/w9va-q159>, 2019.
- 848 Xu, K.-M. & Randall, D. A.: A Semiempirical cloudiness parameterization for use in climate  
849 models. *Journal of the Atmospheric Sciences*, 53(21), 3084–3102.  
850 [https://doi.org/10.1175/1520-0469\(1996\)053\(3084:ASCPFU\)2.0.CO;2](https://doi.org/10.1175/1520-0469(1996)053(3084:ASCPFU)2.0.CO;2), 1996.
- 851 Yang, G., & Slingo, J.: The Diurnal Cycle in the Tropics. *Monthly Weather Review*, 129(4), 784-  
852 801. [https://doi.org/10.1175/1520-0493\(2001\)129<0784:TDCITT>2.0.CO;2](https://doi.org/10.1175/1520-0493(2001)129<0784:TDCITT>2.0.CO;2), 2001.
- 853 Yang, W., Seager, R., Cane, M. A., & Lyon, B.: The annual cycle of East African precipitation.  
854 *Journal of Climate*, 28, 2385–2404. <https://doi.org/10.1175/JCLI-D-14-00484.1>, 2015.
- 855 Zhao, S., & Fu, R.: The influence of convectively coupled Kelvin waves on Atlantic Niños. *Journal*  
856 *of Geophysical Research: Atmospheres*, 127, e2021JD036241.  
857 <https://doi.org/10.1029/2021JD036241>, 2022.
- 858 Zuluaga, M. D., & Houze, R. A.: Evolution of the population of precipitating convective systems  
859 over the equatorial Indian Ocean in active phases of the Madden-Julian Oscillation. *Journal*  
860 *of the Atmospheric Sciences*, 70, 2713–2725. <https://doi.org/10.1175/JAS-D-12-0311.1>,  
861 2013.